Journal of Computational Design and Engineering, 2022, **9**, 1196–1213

DOI: 10.1093/jcde/qwac047
Advance access publication date: 14 May 2022
Research Article

Welding simulation using a reduced order model for efficient residual stress evaluation

Han-Seop Shin and Seung-Hwan Boo*

Division of Naval Architecture and Ocean Systems Engineering, Korea Maritime and Ocean University, 727 Taejong-ro, Yeongdo-gu, Busan 49112, Republic of Korea
*Corresponding author. E-mail: shboo@kmou.ac.kr

Abstract

In this paper, to evaluate the residual stress of welded structures efficiently, we propose a welding simulation method utilizing a reduced order model. To construct the reduced order model, a finite element model is divided into a target part and an omitted part. For the heat transfer analysis, a thermal boundary condition is newly defined and applied to the target part, to compensate for the heat loss induced by neglecting the omitted part. For the thermal elastic plastic analysis, a reduced model for the target part is constructed using the automated static condensation method. The performance of the proposed welding simulation method adopting the reduced order model is verified by solving several welding problems, and it effectively reduces computational costs while predicting the residual stress with little loss of accuracy.

Keywords: welding simulation, residual stress, reduced order model, finite element method, static condensation, substructuring

1 Introduction

Welding is an essential process in many industries. However, it is a known fact that due to the non-uniformity of heating and cooling during the welding process, large stress and strain are produced which may lead to the permanent distortion in a welded joint. Furthermore, the phase transformation of the subjected material during heating and solidification can significantly affect the development of residual stress (Taraphdar *et al.*, 2021). This residual stress can make the joint prone to intergranular stress corrosion cracking, fatigue failure, and brittle fracture. Therefore, to avoid these problems, the quantitative prediction and effective control of residual stress in welded joints should be taken into consideration (Kumar *et al.* 2021; Sauraw *et al.*, 2021). However, experiments and model tests of large structures are very inefficient in terms of both time and cost.

Finite element (FE) simulations are a powerful tool often used to solve these problems by computationally predicting weld residual stresses. Welding simulation using a three-dimensional (3D) FE model can predict the temperature field history and residual stress distribution, which agrees very well with the experimental results (Abid *et al.*, 2005; Deng & Murakawa, 2006; Giri *et al.*, 2015; Pandey *et al.*, 2016, 2018; Taraphdar *et al.*, 2020; Seo & Lee, 2021).

However, welding FE simulations are computationally expensive due to the high non-linearity and transient nature of the welding phenomenon. Moreover, they will require even greater computational costs when considering the recent increase in demand for large, complex welded structures. Therefore, computational efficiency can be regarded as one of the most important issues in welding FE simulations.

To handle the computational cost issues in FE simulations, reduced order model (ROM) methods have been employed in various fields. Zheng *et al.* (1999) used the mode superposition method to perform spectral fatigue analysis of offshore structures efficiently. Mojtahedi *et al.* (2020) proposed an improved ROM method for modal-based structure health monitoring of an offshore jacket-type platform. Roy *et al.* (2021) used matrix interpolation-based parametric model order reduction to increase simulation efficiency for an electrothermal microgripper. For welding FE simulations, traditional static condensation (Guyan, 1965; Wilson, 1974) and superelement techniques (MSC Nastran, 2014) have frequently been employed to construct a ROM. Guirao *et al.* (2009) and Bhatti *et al.* (2014) adopted these techniques to shorten the analysis time for residual stress and strain prediction. In addition, Kawaguchi *et al.* (2011) and Murakawa *et al.* (2015) reduced the computation time by implementing the iterative substructure method (ISM) in which the highly non-linear region close to the local weld zone was iteratively designated as a substructure. In the ISM, the displacement at the boundary between the substructure and the remaining region was computed using the whole FE model, which was considered linear elasticity. This displacement was used as the boundary conditions to solve the substructure and was iteratively corrected by considering the unbalanced force at the boundary.

Unfortunately, the ROM methods used for welding FE simulation in previous studies still have difficulty handling large and complex FE models. For static condensation, the FE model is partitioned into only two parts, the target and the omitted parts, and the omitted part probably has a relatively large number of degrees of freedom (DOFs). The superelement technique, which is mathematically similar to the static condensation method, offers one improvement to address this problem by dividing the omitted part into several substructures. However, because substructures can still have relatively large DOFs (which induce expensive inverse

Received: January 20, 2022. **Revised:** April 19, 2022. **Accepted:** May 8, 2022

matrix computation) and because the substructuring procedure in the physical domain is laborious, great effort is required to construct the ROM.

Recently, high-performance methods to create ROMs for static and dynamic problems (Bennighof & Lehoucq, 2004; Boo & Lee, 2017; Boo & Oh, 2017) are being developed to solve these problems. This will allow the construction of a ROM with remarkable computational efficiency without any consideration of physical substructuring. Therefore, it is necessary to use the high-performance ROM method for calculating large, complex welding FE models more efficiently than with the previous methods. Furthermore, to guarantee the assurance of the ROM, several error estimation techniques have been developed. These techniques can assure the ROM without solving the global model (Boo *et al.*, 2015, 2016).

In this study, we aim to develop an efficient welding FE simulation method (using the ROM) for both thermal and mechanical analyses. The new features of the proposed method are as follows: For the thermal analysis, we develop a new thermal boundary condition for the interface boundary of the target part to construct the thermal ROM. For the mechanical analysis, we construct a mechanical ROM using the automated static condensation (ASC) method, that is, the high-performance ROM method. Then, only the non-linearity of the ROM needs to be iteratively updated to perform the welding FE simulation efficiently.

In Section 2, we briefly introduce the formulation of heat transfer analysis and thermal elastic plastic analysis for the welding FE simulation. In Section 3, the partitioning of the global FE model is introduced, and the formulations and condensation procedures of the proposed method are described for both heat transfer analysis and thermal elastic plastic analysis. In Section 4, the performance of the proposed method in terms of accuracy and computational efficiency is demonstrated through several welding FE simulations.

2 Formulations of the Welding Analysis

In this section, we briefly review the 3D thermo-mechanical formulation of the welding analysis, which consists of sequentially coupled heat transfer analysis and thermal elastic plastic analysis. The phase change of the material is not considered in the analyses.

2.1 Heat transfer analysis

The formulations of heat transfer analysis are briefly introduced in this section, see references (Shanghvi & Michaelis, 2002; Bathe, 2006; Anca *et al.*, 2011) for detailed derivations. Considering the heat transfer problem for a 3D body in which material obeys Fourier's law of heat conduction, the heat flow equilibrium equation (Bathe, 2006) is defined as

$$\frac{\partial}{\partial x}\left(k_x\frac{\partial\theta}{\partial x}\right)+\frac{\partial}{\partial y}\left(k_y\frac{\partial\theta}{\partial y}\right)+\frac{\partial}{\partial z}\left(k_z\frac{\partial\theta}{\partial z}\right)+q^B=0, \tag{1}$$

and its tensorial form can be written as

$$(k_i\,\theta_{,i})_{,i}+q^B=0, \tag{2}$$

where k is the thermal conductivity, q^B is the rate of heat generated per unit volume, and θ is the temperature.

From the heat transfer body definition shown in Fig. 1, the following boundary conditions are defined as

$$\theta|_{S^\theta}=\theta^{S^\theta},\quad k_n\cdot\theta_{,n}\big|_{S^q}=q^S,\quad k_n\cdot\theta_{,n}\big|_{S^c}=h^e(\theta^e-\theta), \tag{3}$$

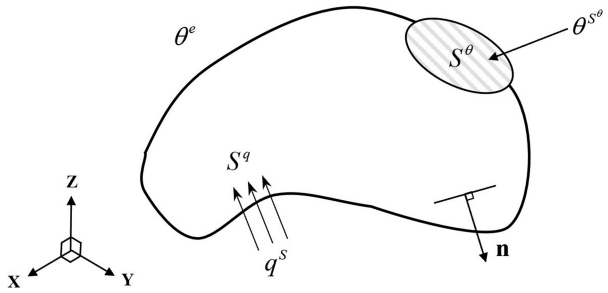

Figure 1: Heat transfer body definition.

where S^θ is the specific surface to which the prescribed temperature θ^{S^θ} is applied. Here, S^q is the heat flux input surface of the prescribed heat flux q^S, and S^c is the convection surface included in S^q. The vector $\mathbf{n}$ is the outward unit normal vector of the surface and n is its coordinate axis. The term θ^e is the environmental temperature whose heat transfer coefficient is h^e.

After applying the principle of virtual temperatures (Bathe, 2006) and the boundary conditions in Equation (3), a weak form of the governing equation is obtained as

$$\int_V \bar{\boldsymbol{\theta}}'^T\,\mathbf{k}\,\boldsymbol{\theta}'\,dV=\int_V\bar{\theta}q^B dV+\int_{S^q}\bar{\theta}q^S dS+\int_{S^c}\bar{\theta}h^e(\theta^e-\theta)dS,$$

$$\text{with}\quad \mathbf{k}=\begin{bmatrix}k_x&0&0\\0&k_y&0\\0&0&k_z\end{bmatrix},\quad \boldsymbol{\theta}'^T=\begin{bmatrix}\frac{\partial\theta}{\partial x}&\frac{\partial\theta}{\partial y}&\frac{\partial\theta}{\partial z}\end{bmatrix}, \tag{4}$$

where $\mathbf{k}$ is the thermal conductivity matrix, and $\boldsymbol{\theta}'$ is the temperature gradient vector. The overbar indicates the virtual terms.

After the FE discretization, for an element m with n nodes, the temperature vector $\boldsymbol{\theta}_m$ and the temperature gradient vector $\boldsymbol{\theta}'_m$ are defined by

$$\boldsymbol{\theta}_m=\mathbf{H}_m\,\boldsymbol{\theta},\quad \boldsymbol{\theta}'_m=\mathbf{B}_m\,\boldsymbol{\theta}\quad\text{with}\quad \boldsymbol{\theta}^T=[\theta_1,\,\theta_2,\,\cdots,\,\theta_n], \tag{5}$$

in which $\mathbf{H}_m$ is the element temperature interpolation matrix, and $\mathbf{B}_m$ is the element temperature-gradient interpolation matrix.

Substituting Equations (5) into (4), and after assembling for the total elements, we can obtain the FE governing equation of linear steady-state heat transfer analysis as follows

$$(\mathbf{k}^k+\mathbf{k}^e)\boldsymbol{\theta}=\mathbf{Q}^B+\mathbf{Q}^S+\mathbf{Q}^e,\quad\text{with}\quad \mathbf{k}^k=\sum_m\int_{V_m}\mathbf{B}_m^T\,\mathbf{k}_m\,\mathbf{B}_m\,dV_m,$$

$$\mathbf{k}^e=\sum_m\int_{S_m^c}h_m^e\,\mathbf{H}_m^T\,\mathbf{H}_m\,dS_m,\quad \mathbf{Q}^B=\sum_m\int_{V_m}\mathbf{H}_m^T\,q_m^B\,dV_m,$$

$$\mathbf{Q}^S=\sum_m\int_{S_m^q}\mathbf{H}_m^T\,q_m^S\,dS_m,\quad \mathbf{Q}^e=\sum_m\int_{S_m^c}h_m^e\,\mathbf{H}_m^T\,\mathbf{H}_m\,\boldsymbol{\theta}^e\,dS_m, \tag{6}$$

where $\mathbf{k}^k$ and $\mathbf{k}^e$ denote the conductivity and convection matrices, respectively, whereas $\mathbf{Q}^B$ and $\mathbf{Q}^S$ denote the nodal heat flow input vector corresponding to q^B and q^S, respectively. Here, $\mathbf{Q}^e$ is the nodal heat flow contribution due to convection.

In the transient state, it is important to include a term considering the rate at which heat is stored in the material. This rate of heat absorption is given as

$$q^c=\rho c\,\dot{\theta}, \tag{7}$$

where ρ and c are the material density and the material specific heat capacity, respectively, and $\dot{\theta}$ is the time derivative of temperature. Here, q^c can be understood to be part of the heat generated and must be subtracted from q^B in Equation (4).

Thus, for element m, the time-derived temperature vector $\dot{\boldsymbol{\theta}}_m$ is defined as

$$\dot{\boldsymbol{\theta}}_m(t) = \mathbf{H}_m\,\dot{\boldsymbol{\theta}}\,(t), \tag{8}$$

and $\mathbf{Q}^{\mathrm{B}}$ in Equation (6) is redefined using Equations (7) and (8) as

$$\mathbf{Q}^{\mathrm{B}} = \sum_m \int_{V_m} \mathbf{H}_m^T \left(q_m^{\mathrm{B}} - (\rho c)_m \mathbf{H}_m \dot{\boldsymbol{\theta}}\right) \mathrm{d}V_m\,. \tag{9}$$

Substituting Equations (9) into (6), we can obtain the FE heat flow equilibrium equation considered in transient condition as follows

$$\mathbf{C}\dot{\boldsymbol{\theta}} + \mathbf{k}\boldsymbol{\theta} = \mathbf{Q} \quad \text{with} \quad \mathbf{C} = \sum_m \int_{V_m} \mathbf{H}_m^T (\rho c)_m \mathbf{H}_m \,\mathrm{d}V_m,$$
$$\mathbf{k} = \mathbf{k}^k + \mathbf{k}^e, \quad \mathbf{Q} = \mathbf{Q}^{\mathrm{B}} + \mathbf{Q}^{\mathrm{S}} + \mathbf{Q}^e, \tag{10}$$

where $\mathbf{C}$ and $\mathbf{k}$ are the heat capacity matrix and the conductivity matrix, respectively, and $\mathbf{Q}$ is the nodal heat flow vector.

Assuming the conditions at time t have been calculated, and considering that the time stepping is merely used to describe the heat flow loading, the FE governing equation in Equation (10) at time $t + \Delta t$ is written as

$${}^{t+\Delta t}\mathbf{C}\,{}^{t+\Delta t}\dot{\boldsymbol{\theta}} + {}^{t+\Delta t}\mathbf{k}\,{}^{t+\Delta t}\boldsymbol{\theta} = {}^{t+\Delta t}\mathbf{Q}, \tag{11}$$

where ${}^{t+\Delta t}\boldsymbol{\theta}$ and ${}^{t+\Delta t}\mathbf{Q}$ are the nodal temperature and heat flow vectors at time $t + \Delta t$.

For the non-linear analysis, all variables in Equation (11) are updated in each iteration, and the solution is obtained by incrementally decomposing the nodal temperatures as

$${}^{t+\Delta t}\mathbf{C}^{(i)}\,{}^{t+\Delta t}\dot{\boldsymbol{\theta}}^{(i)} + {}^{t+\Delta t}\mathbf{k}^{(i-1)}\,{}^{t+\Delta t}\boldsymbol{\theta}^{(i)} = {}^{t+\Delta t}\mathbf{Q}$$
$$\text{with} \quad {}^{t+\Delta t}\boldsymbol{\theta}^{(i)} = {}^{t+\Delta t}\boldsymbol{\theta}^{(i-1)} + \Delta\boldsymbol{\theta}^{(i)}, \tag{12}$$

where ${}^{t+\Delta t}\boldsymbol{\theta}^{(i)}$ and $\Delta\boldsymbol{\theta}^{(i)}$ are the nodal temperature vector and incremental nodal temperature vector at the end of iteration i.

Using Equation (12) and the Newton–Raphson iteration, the FE governing equation of the non-linear transient heat transfer analysis adopting the implicit time integration procedure is obtained as

$${}^{t+\Delta t}\mathbf{C}^{(i)}\,{}^{t+\Delta t}\dot{\boldsymbol{\theta}}^{(i)} + {}^{t+\Delta t}\mathbf{k}^{(i-1)}\Delta\boldsymbol{\theta}^{(i)} = {}^{t+\Delta t}\tilde{\mathbf{Q}}^{(\mathbf{i-1})}, \tag{13}$$

where ${}^{t+\Delta t}\tilde{\mathbf{Q}}^{(\mathbf{i-1})}$ is the vector of nodal heat flows corresponding to time $t + \Delta t$ and iteration $(i - 1)$.

From Equations (12) and (13), ${}^{t+\Delta t}\tilde{\mathbf{Q}}^{(\mathbf{i-1})}$ can be expressed as

$${}^{t+\Delta t}\tilde{\mathbf{Q}}^{(i-1)} = {}^{t+\Delta t}\mathbf{Q}^{\mathrm{B}} + {}^{t+\Delta t}\mathbf{Q}^{\mathrm{S}} + {}^{t+\Delta t}\mathbf{Q}^{\mathbf{e}(i-1)} - {}^{t+\Delta t}\mathbf{Q}^{\mathbf{k}(i-1)},$$
$$\text{with} \quad {}^{t+\Delta t}\mathbf{Q}^{\mathbf{e}(i-1)} = \sum_m \int_{S_m^{\mathrm{S}}} {}^{t+\Delta t}h_m^{e\,(i-1)}\,\mathbf{H}_m^T \left[\mathbf{H}_m \left({}^{t+\Delta t}\boldsymbol{\theta}^e - {}^{t+\Delta t}\boldsymbol{\theta}^{(i-1)}\right)\right] \mathrm{d}S_m,$$
$${}^{t+\Delta t}\mathbf{Q}^{\mathbf{k}(i-1)} = \sum_m \int_{V_m} \mathbf{B}_m^T \left[{}^{t+\Delta t}\mathbf{k}_m^{(i-1)}\,\mathbf{B}_m\,{}^{t+\Delta t}\boldsymbol{\theta}^{(i-1)}\right] \mathrm{d}V_m. \tag{14}$$

Employing the Euler backward method (Bathe, 2006), we have

$${}^{t+\Delta t}\dot{\boldsymbol{\theta}}^{(i)} = \frac{{}^{t+\Delta t}\boldsymbol{\theta}^{(i-1)} + \Delta\boldsymbol{\theta}^{(i)} - {}^{t}\boldsymbol{\theta}}{\Delta t}, \tag{15}$$

and Equation (15) can be rewritten as

$$\left({}^{t+\Delta t}\mathbf{k}^{(i-1)} + \frac{1}{\Delta t}\,{}^{t+\Delta t}\mathbf{C}^{(i)}\right)\Delta\boldsymbol{\theta}^{(i)} = {}^{t+\Delta t}\tilde{\mathbf{Q}}^{(i-1)} - {}^{t+\Delta t}\mathbf{C}^{(i)}\,{}^{t+\Delta t}\dot{\boldsymbol{\theta}}^{(i-1)},$$
$$\text{with} \quad {}^{t+\Delta t}\dot{\boldsymbol{\theta}}^{(i-1)} = \frac{{}^{t+\Delta t}\boldsymbol{\theta}^{(i-1)} - {}^{t}\boldsymbol{\theta}}{\Delta t}. \tag{16}$$

For the solution, Equation (16) can be further linearized using

$$\left({}^{t+\Delta t}\mathbf{k}^{(i-1)} + \frac{1}{\Delta t}\,{}^{t+\Delta t}\mathbf{C}^{(i-1)}\right)\Delta\boldsymbol{\theta}^{(i)} = {}^{t+\Delta t}\tilde{\mathbf{Q}}^{(\mathbf{i-1})} - {}^{t+\Delta t}\mathbf{C}^{(i-1)}\,{}^{t+\Delta t}\dot{\boldsymbol{\theta}}^{(i-1)}, \tag{17}$$

and from Equation (17), the incremental temperature vector $\Delta\boldsymbol{\theta}^{(i)}$ to be applied to the thermal elastic plastic analysis can be calculated at each time step of the analysis.

2.2 Thermal elastic plastic analysis

In the thermal elastic plastic analysis, the displacement and stress increments will be determined at each time step by referring to the temperature field history ${}^{t+\Delta t}\boldsymbol{\theta}^{(i)}$ and $\Delta\boldsymbol{\theta}^{(i)}$ obtained in the previous section. The material behavior is based on the stress–strain relationship for the thermal elastic plastic material.

The stress–strain relation for elastic material is defined as

$$\boldsymbol{\sigma}_m = \mathbf{D}_m^e\,\boldsymbol{\varepsilon}_m, \tag{18}$$

where $\boldsymbol{\sigma}_m$ and $\boldsymbol{\varepsilon}_m$ are the stress and strain vectors for element m, respectively, and $\mathbf{D}_m^e$ is the elastic stress–strain matrix (Ueda & Yamakawa, 1971).

Assuming the initial strain $\boldsymbol{\varepsilon}^0$ exists and is considered in Equation (18), the elastic stress–strain relation can be rewritten with consideration of the strain difference as follows,

$$\boldsymbol{\sigma}_m = \mathbf{D}_m^e\,\left(\boldsymbol{\varepsilon}_m - \boldsymbol{\varepsilon}_m^0\right). \tag{19}$$

For a general 3D element m, the force equilibrium equation (Bathe, 2006) can be defined in matrix-vector form for a unit volume by

$$\nabla\cdot\boldsymbol{\sigma}_m + \mathbf{f}_m^{\mathrm{B}} = \mathbf{0}, \tag{20}$$

where $\mathbf{f}_m^{\mathrm{B}}$ is the body force vector for element m, and ∇ is the spatial gradient operator.

For the element m with n nodes, the strain vector $\boldsymbol{\varepsilon}_m$ and the displacement vector $\mathbf{u}_m$ can be defined as

$$\boldsymbol{\varepsilon}_m = \mathbf{L}_m\,\mathbf{u}, \quad \mathbf{u}_m = \mathbf{N}_m\,\mathbf{u} \quad \text{with} \quad \mathbf{u}^{\mathrm{T}} = [u_1,\,u_2,\,\cdots,\,u_n], \tag{21}$$

in which $\mathbf{u}$ is the nodal displacement vector. Here, $\mathbf{L}_m$ is the strain-displacement matrix and $\mathbf{N}_m$ is the displacement interpolation matrix.

Applying the virtual displacement vector $\tilde{\mathbf{u}}$ into Equation (20), a key concept of the principle of virtual work, we can obtain

$$\int_{V_m} \tilde{\mathbf{u}}_m^T \left(\nabla\cdot\boldsymbol{\sigma}_m + \mathbf{f}_m^{\mathrm{B}}\right) \mathrm{d}V_m = 0, \tag{22}$$

and then, considering the integration by part (Bathe, 2006) to the left-hand side, it can be rewritten as

$$\int_{V_m} \tilde{\boldsymbol{\varepsilon}}_m^T\,\boldsymbol{\sigma}_m\,\mathrm{d}V_m = \int_{V_m} \tilde{\mathbf{u}}_m^T\,\mathbf{f}_m^{\mathrm{B}}\,\mathrm{d}V_m + \int_{S_m} \tilde{\mathbf{u}}_m^T\,\mathbf{f}_m^{\mathrm{S}}\,\mathrm{d}S_m$$
$$\text{with} \quad \mathbf{f}_m^{\mathrm{S}} = \boldsymbol{\sigma}_m\,\mathbf{n}, \tag{23}$$

where $\mathbf{f}_m^{\mathrm{S}}$ is the surface force vector for element m.

Substituting Equations (19) and (21) into (23), and after assembling for the total elements, the following static equation is de-

fined as

$$\mathbf{Ku} = \mathbf{F}, \quad \text{with} \quad \mathbf{K} = \sum_m \int_{V_m} \mathbf{L}_m^T \mathbf{D}_m^e \mathbf{L}_m \, dV_m,$$
$$\mathbf{F} = \sum_m \int_{V_m} \mathbf{N}_m^T \mathbf{f}_m^B \, dV_m + \sum_m \int_{S_m} \mathbf{N}_m^T \mathbf{f}_m^S \, dS_m$$
$$+ \sum_m \int_{V_m} \mathbf{L}_m^T \mathbf{D}_m^e \boldsymbol{\varepsilon}_m^0 \, dV_m, \tag{24}$$

where $\mathbf{K}$ and $\mathbf{F}$ are the stiffness matrix and nodal force vector for the FE model.

Note that, the stress–strain relationship for thermal elastic plastic material can be considered to change linearly in a time increment. The solution at each time increment is obtained by performing static analysis using the pre-calculated increment as the initial condition (Shanghvi & Michaleris, 2002).

Assuming small deformation thermoelastic plasticity (Wang *et al.*, 2008), the incremental total strain $\Delta\boldsymbol{\varepsilon}_m$ can be decomposed into the incremental elastic, plastic, and thermal strain vectors ($\Delta\boldsymbol{\varepsilon}_m^e$, $\Delta\boldsymbol{\varepsilon}_m^p$, $\Delta\boldsymbol{\varepsilon}_m^{th}$) as follows:

$$\Delta\boldsymbol{\varepsilon}_m = \Delta\boldsymbol{\varepsilon}_m^e + \Delta\boldsymbol{\varepsilon}_m^p + \Delta\boldsymbol{\varepsilon}_m^{th}. \tag{25}$$

Considering the plasticity of the material, the incremental plastic stress–strain relation (Ueda and Yamakawa, 1971) can be defined as

$$\Delta\boldsymbol{\sigma}_m = \mathbf{D}_m^p \left(\Delta\boldsymbol{\varepsilon}_m - \Delta\boldsymbol{\varepsilon}_m^0\right), \tag{26}$$

in which $\Delta\boldsymbol{\sigma}_m$ and $\Delta\boldsymbol{\varepsilon}_m$ are the incremental stress and total strain vectors, $\mathbf{D}_m^p$ is the plastic stress–strain matrix, and $\Delta\boldsymbol{\varepsilon}_m^0$ is the incremental initial strain vector, respectively.

In the case of welding analysis, the incremental initial strain vector $\Delta\boldsymbol{\varepsilon}_m^0$ in Equation (26) can be regarded as the incremental thermal strain vector $\Delta\boldsymbol{\varepsilon}_m^{th}$ (Ueda & Yamakawa, 1971), and replaced as follows:

$$\Delta\boldsymbol{\varepsilon}_m^0 = \Delta\boldsymbol{\varepsilon}_m^{th} = \boldsymbol{\alpha}_m \, \Delta\boldsymbol{\theta}_m, \tag{27}$$

where $\Delta\boldsymbol{\varepsilon}_m^{th}$ is calculated with the heat expansion coefficient $\boldsymbol{\alpha}_m$ and the incremental temperature vector $\Delta\boldsymbol{\theta}_m$.

Using Equations (19), (26), and (27), the incremental stress–strain relation for thermal elastic plastic material can be defined as

$$\Delta\boldsymbol{\sigma}_m = \mathbf{D}_m \left(\Delta\boldsymbol{\varepsilon}_m - \Delta\boldsymbol{\varepsilon}_m^{th}\right), \tag{28}$$

where $\mathbf{D}_m$ is the incremental stress–strain matrix, and it can be defined as the elastic stress–strain matrix $\mathbf{D}_m^e$ and the plastic stress–strain matrix $\mathbf{D}_m^p$ according to the elasticity and plasticity.

Assuming the temperature dependence of the mechanical material properties, Equation (28) can be rewritten as

$$\Delta\boldsymbol{\sigma}_m = \mathbf{D}_m \Delta\boldsymbol{\varepsilon}_m - \mathbf{C}_m \Delta\boldsymbol{\theta}_m, \tag{29}$$

where $\mathbf{C}_m$ is the thermal matrix (Ueda & Yamakawa, 1971; Shanghvi & Michaleris, 2002; Wang *et al.*, 2008) consisting of the effects of the temperature change $\Delta\boldsymbol{\theta}_m$ on the stress increment $\Delta\boldsymbol{\sigma}_m$.

Considering the incremental forms of Equation (23), the following equation can be obtained

$$\int_{V_m} \bar{\boldsymbol{\varepsilon}}^T \, \Delta\boldsymbol{\sigma}_m \, dV_m = \int_{V_m} \bar{\mathbf{u}}^T \, \Delta\mathbf{f}_m^B \, dV_m + \int_{S_m} \bar{\mathbf{u}}^T \, \Delta\mathbf{f}_m^S \, dS_m, \tag{30}$$

where $\Delta\mathbf{f}_m^B$ and $\Delta\mathbf{f}_m^S$ are the incremental body and surface force vectors for element m, respectively.

From Equations (5) and (21), the incremental forms of strain, displacement, and temperature vectors ($\Delta\boldsymbol{\varepsilon}_m$, $\Delta\mathbf{u}_m$ and $\Delta\boldsymbol{\theta}_m$) can be defined as

$$\Delta\boldsymbol{\varepsilon}_m = \mathbf{L}_m \, \Delta\mathbf{u}, \quad \Delta\mathbf{u}_m = \mathbf{N}_m \, \Delta\mathbf{u}, \quad \Delta\boldsymbol{\theta}_m = \mathbf{H}_m \, \Delta\boldsymbol{\theta}$$
$$\text{with} \quad \Delta\boldsymbol{\theta}^T = [\Delta\theta_1, \, \Delta\theta_2, \, \cdots, \, \Delta\theta_n], \tag{31}$$

in which $\Delta\mathbf{u}$ is the incremental nodal displacement vectors, and $\Delta\boldsymbol{\theta}$ is the incremental nodal temperature vector.

Substituting the virtual form of Equations (31) into (30), we can obtain the following equation

$$\int_{V_m} \mathbf{L}_m^T \, \Delta\boldsymbol{\sigma}_m \, dV_m = \int_{V_m} \mathbf{N}_m^T \, \Delta\mathbf{f}_m^B \, dV_m + \int_{S_m} \mathbf{N}_m^T \, \Delta\mathbf{f}_m^S \, dS_m. \tag{32}$$

Finally, after assembling the total elements for Equation (32), the FE governing equation (Wang *et al.*, 2008) of the thermal elastic plastic analysis is defined as

$$\mathbf{K} \, \Delta\mathbf{u} = \Delta\mathbf{F}, \quad \text{with} \quad \mathbf{K} = \sum_m \int_{V_m} \mathbf{L}_m^T \mathbf{D}_m \mathbf{L}_m \, dV_m,$$
$$\Delta\mathbf{F} = \sum_m \int_{V_m} \mathbf{N}_m^T \, \Delta\mathbf{f}_m^B \, dV_m + \sum_m \int_{S_m} \mathbf{N}_m^T \, \Delta\mathbf{f}_m^S \, dS_m$$
$$+ \sum_m \int_{V_m} \mathbf{L}_m^T \left[\mathbf{C}_m \mathbf{H}_m \, \Delta\boldsymbol{\theta}\right] dV_m, \tag{33}$$

where $\mathbf{K}$ is the stiffness matrix, and $\Delta\mathbf{F}$ is the incremental nodal force vector.

Applying the Newton–Raphson iteration into Equation (33), we can obtain the incremental non-linear FE governing equation as follows:

$$\mathbf{K}^{(j-1)} \Delta\mathbf{u}^{(j)} = \mathbf{F}^{(j)} - \mathbf{F}^{(j-1)}, \tag{34}$$

in which $\Delta\mathbf{u}^{(j)}$ and $\mathbf{F}^{(j)}$ are the incremental nodal displacement and nodal force vectors in iteration j, respectively.

After solving Equation (34), the nodal displacement vector at each step can be calculated using

$$\mathbf{u}^{(j)} = \mathbf{u}^{(j-1)} + \Delta\mathbf{u}^{(j)}, \tag{35}$$

and then, the updated stress distributions at each step can be calculated as follows:

$$\Delta\boldsymbol{\sigma}^{(j)} = \sum_m \mathbf{D}_m^{(j-1)} \mathbf{L}_m \, \Delta\mathbf{u}^{(j)} - \sum_m \mathbf{C}_m^{(j-1)} \mathbf{H}_m \, \Delta\boldsymbol{\theta}^{(i)}, \tag{36}$$
$$\boldsymbol{\sigma}^{(j)} = \boldsymbol{\sigma}^{(j-1)} + \Delta\boldsymbol{\sigma}^{(j)}, \tag{37}$$

in which the terms related to the temperatures are $\mathbf{C}_m^{(j-1)}$ and $\Delta\boldsymbol{\theta}^{(i)}$. Here, $\mathbf{C}_m^{(j-1)}$ is calculated by considering the temperature field distribution ${}^{t+\Delta t}\boldsymbol{\theta}^{(i)}$. As mentioned before, the temperature field history ${}^{t+\Delta t}\boldsymbol{\theta}^{(i)}$ and $\Delta\boldsymbol{\theta}^{(i)}$ are obtained from the heat transfer analysis described in Section 2.1.

However, the global FE model for welding analysis is often considerably inefficient due to transient conditions and non-linear iterations with a large number of DOFs. Fortunately, in this simulation, the non-linearity part is a relatively small portion compared to the global model. Therefore, it is necessary to use a ROM for the welding analysis, which can give powerful computational efficiency.

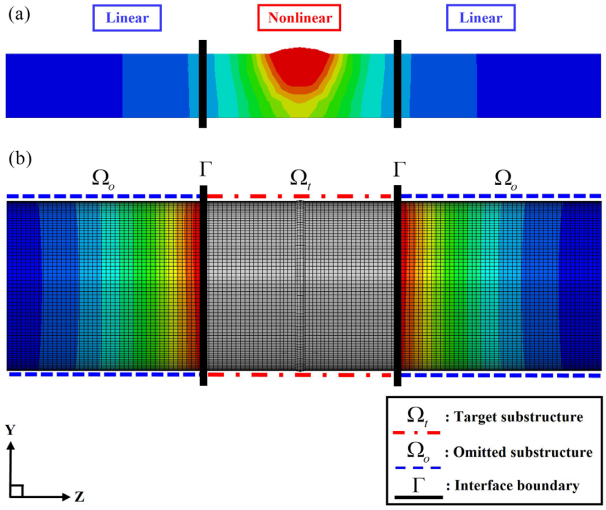

Figure 2: Partitioning scheme of the proposed method. (a) Dividing non-linear and linear regions in the welding FE model. (b) Substructuring Ω_t and Ω_o with the interface boundary Γ.

3 ROM for Welding Analysis

In this section, we introduce the partitioning scheme that is a prerequisite condition before applying the proposed method, and a new thermal boundary condition is introduced for conducting the heat transfer analysis more efficiently. Then, we introduce a procedure to construct the ROM for the thermal elastic plastic analysis.

3.1 Partitioning scheme of the proposed method

The welding FE model can be divided into a linear region and a non-linear region as shown in Fig. 2a. The partitioning of the FE model can be carried out either by assuming a temperature at which elements have no plastic strains (Kawaguchi *et al.*, 2011; Bhatti *et al.*, 2014; Murakawa *et al.*, 2015) or by selecting an arbitrary region away from the local weld zone (Guirao *et al.*, 2009).

In this study, the FE model is partitioned into two parts, the "target" part Ω_t and the "omitted" part Ω_o, as shown in Fig. 2b. Here, all areas where non-linearity occurs, that is, where the welding arc passes and the region enough away from the welding arc are designated as the target part Ω_t, and the remaining regions are designated as the omitted part Ω_o. The interface boundary Γ can be defined using the coupled DOFs between Ω_t and Ω_o.

3.2 Thermal boundary condition

From Equation (13), the formulation of the non-linear thermal governing equation, based on the partitioning scheme described earlier, can be defined as

$$\mathbf{C}^{(i)}\dot{\boldsymbol{\theta}}^{(i)}+\mathbf{k}^{(i-1)}\Delta\boldsymbol{\theta}^{(i)}=\tilde{\mathbf{Q}}^{(i-1)},$$

with

$$\mathbf{C}^{(i)}=\left[\begin{array}{c|c}\mathbf{C}_o^{(i)} & \mathbf{C}_{ot}^{(i)}\\ \hline \mathbf{C}_{to}^{(i)} & \mathbf{C}_t^{(i)}\end{array}\right],\quad \dot{\boldsymbol{\theta}}^{(i)}=\left[\begin{array}{c}\dot{\boldsymbol{\theta}}_o^{(i)}\\ \hline \dot{\boldsymbol{\theta}}_t^{(i)}\end{array}\right],\quad \mathbf{k}^{(i-1)}=\left[\begin{array}{c|c}\mathbf{k}_o^{(i-1)} & \mathbf{k}_{ot}^{(i-1)}\\ \hline \mathbf{k}_{to}^{(i-1)} & \mathbf{k}_t^{(i-1)}\end{array}\right], \tag{38}$$

$$\Delta\boldsymbol{\theta}^{(i)}=\left[\begin{array}{c}\Delta\boldsymbol{\theta}_o^{(i)}\\ \hline \Delta\boldsymbol{\theta}_t^{(i)}\end{array}\right],\quad \tilde{\mathbf{Q}}^{(i-1)}=\left[\begin{array}{c}\tilde{\mathbf{Q}}_o^{(i-1)}\\ \hline \tilde{\mathbf{Q}}_t^{(i-1)}\end{array}\right],$$

in which subscript o and t denote the omitted part Ω_o and target part Ω_t, respectively. Here, ot and to indicate the coupled nodes between the omitted and target parts, and all variables are expressed without the superscript $t+\Delta t$ for convenience.

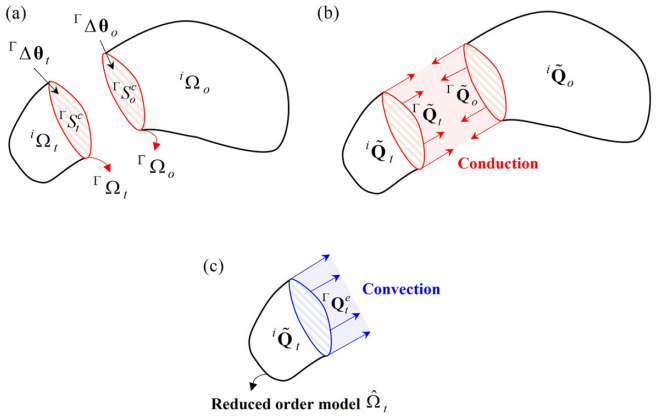

Figure 3: Heat flow of the partitioned body. (a) Decomposing substructures into the interior i and the interface boundary Γ. (b) Heat flow decomposition for the substructures. (c) Replacing the conduction term ${}^{\Gamma}\tilde{\mathbf{Q}}_t$ with the convection term ${}^{\Gamma}\mathbf{Q}_t^e$.

Expanding the first and second row in Equation (38), the thermal governing equations for the target and omitted parts can be defined separately as

$$\left(\mathbf{C}_o^{(i)}\dot{\boldsymbol{\theta}}_o^{(i)}+\mathbf{k}_o^{(i-1)}\Delta\boldsymbol{\theta}_o^{(i)}\right)+\left(\mathbf{C}_{ot}^{(i)}\dot{\boldsymbol{\theta}}_t^{(i)}+\mathbf{k}_{ot}^{(i-1)}\Delta\boldsymbol{\theta}_t^{(i)}\right)=\tilde{\mathbf{Q}}_o^{(i-1)}, \tag{39a}$$

$$\left(\mathbf{C}_{to}^{(i)}\dot{\boldsymbol{\theta}}_o^{(i)}+\mathbf{k}_{to}^{(i-1)}\Delta\boldsymbol{\theta}_o^{(i)}\right)+\left(\mathbf{C}_t^{(i)}\dot{\boldsymbol{\theta}}_t^{(i)}+\mathbf{k}_t^{(i-1)}\Delta\boldsymbol{\theta}_t^{(i)}\right)=\tilde{\mathbf{Q}}_t^{(i-1)}. \tag{39b}$$

Then, as shown in Fig. 3, the heat flow vectors $\tilde{\mathbf{Q}}_o^{(i-1)}$ and $\tilde{\mathbf{Q}}_t^{(i-1)}$ in Equation (39) can be decomposed into the interior i and its interface boundary Γ (Anca *et al.*, 2011) as follows:

$$\tilde{\mathbf{Q}}_o^{(i-1)}={}^{i}\tilde{\mathbf{Q}}_o^{(i-1)}+{}^{\Gamma}\tilde{\mathbf{Q}}_o^{(i-1)}\quad\text{with}\quad {}^{i}\tilde{\mathbf{Q}}_o^{(i-1)}={}^{i}\mathbf{Q}_o^{e(i-1)}-{}^{i}\mathbf{Q}_o^{k(i-1)},$$
$${}^{\Gamma}\tilde{\mathbf{Q}}_o^{(i-1)}=-{}^{\Gamma}\mathbf{Q}_o^{k(i-1)}, \tag{40a}$$

$$\tilde{\mathbf{Q}}_t^{(i-1)}={}^{i}\tilde{\mathbf{Q}}_t^{(i-1)}+{}^{\Gamma}\tilde{\mathbf{Q}}_t^{(i-1)}$$
$$\text{with}\quad {}^{i}\tilde{\mathbf{Q}}_t^{(i-1)}={}^{i}\mathbf{Q}_t^{B}+{}^{i}\mathbf{Q}_t^{S}+{}^{i}\mathbf{Q}_t^{e(i-1)}-{}^{i}\mathbf{Q}_t^{k(i-1)},$$
$${}^{\Gamma}\tilde{\mathbf{Q}}_t^{(i-1)}=-{}^{\Gamma}\mathbf{Q}_t^{k(i-1)}, \tag{40b}$$

where ${}^{i}\tilde{\mathbf{Q}}_o^{(i-1)}$ and ${}^{i}\tilde{\mathbf{Q}}_t^{(i-1)}$ are the interior heat flow vectors of the omitted and target parts, except for the interface heat flow vectors ${}^{\Gamma}\tilde{\mathbf{Q}}_o^{(i-1)}$ and ${}^{\Gamma}\tilde{\mathbf{Q}}_t^{(i-1)}$, respectively. Here, there is no heat flow

input vector in the internal heat flow vector ${}^{i}\tilde{\mathbf{Q}}_{o}^{(i-1)}$ due to the partitioning.

Note that, considering the continuity of the temperature at the interface boundary Γ, the interface heat flow vector ${}^{\Gamma}\tilde{\mathbf{Q}}_{t}^{(i-1)}$ can be understood as the heat loss from the target part Ω_t, and in the case where only the target part Ω_t is considered independently, the heat flow vectors ${}^{\Gamma}\tilde{\mathbf{Q}}_{o}^{(i-1)}$ and ${}^{\Gamma}\tilde{\mathbf{Q}}_{t}^{(i-1)}$ generated by the heat conduction are eliminated. Therefore, to consider the eliminated terms, we need to adequately compensate the conduction term by applying the convection term as a thermal boundary condition for the target part interface boundary ${}^{\Gamma}\Omega_t$, as shown in Fig. 3c.

To convert the conduction term into the convection term, considering only the convection term in Equations (13) and (14), the following equation is obtained:

$$\mathbf{Q}^{e(\mathbf{i-1})} = \mathbf{k}^{e(i-1)}\,\Delta\boldsymbol{\theta}^{(i)} \tag{41}$$

and we can use this convection term as a thermal boundary condition that is applied to the target part interface boundary ${}^{\Gamma}\Omega_t$, as follows

$${}^{\Gamma}\mathbf{Q}_{t}^{e(i-1)} = {}^{\Gamma}\mathbf{k}_{t}^{e(i-1)}\,{}^{\Gamma}\Delta\boldsymbol{\theta}_{t}^{(i)}, \tag{42}$$

where ${}^{\Gamma}\mathbf{Q}_{t}^{e(i-1)}$ and ${}^{\Gamma}\mathbf{k}_{t}^{e(i-1)}$ are the newly defined heat flow vector and convection matrix for the convection surface ${}^{\Gamma}S_{t}^{c}$ with the heat transfer coefficient ${}^{\Gamma}h_{t}^{e(i-1)}$, and ${}^{\Gamma}\Delta\boldsymbol{\theta}_{t}^{(i)}$ is the corresponding temperature vector. Here, the procedure for calculation of ${}^{\Gamma}h_{t}^{e(i-1)}$ is explained and the application of ${}^{\Gamma}S_{t}^{c}$ to the welding FE models will be described in detail in Section 4.

Then, substituting ${}^{\Gamma}\mathbf{Q}_{t}^{e(i-1)}$ in Equation (42) into ${}^{\Gamma}\tilde{\mathbf{Q}}_{t}^{(i-1)}$ in Equation (40b), the heat flow vector $\tilde{\mathbf{Q}}_{t}^{(i-1)}$ can be approximated as

$$\begin{aligned}
&\tilde{\mathbf{Q}}_{t}^{(i-1)} \approx \hat{\mathbf{Q}}_{t}^{(i-1)} = {}^{i}\tilde{\mathbf{Q}}_{t}^{(i-1)} + {}^{\Gamma}\mathbf{Q}_{t}^{e(i-1)},\\
&\text{with}\quad {}^{i}\tilde{\mathbf{Q}}_{t}^{(i-1)} = \mathbf{C}_{t}^{(i)}\dot{\boldsymbol{\theta}}_{t}^{(i)} + \mathbf{k}_{t}^{(i-1)}\Delta\boldsymbol{\theta}_{t}^{(i)},\\
&{}^{\Gamma}\mathbf{Q}_{t}^{e(i-1)} = {}^{\Gamma}\mathbf{k}_{t}^{e(i-1)}\,{}^{\Gamma}\boldsymbol{\Delta\theta}_{t}^{(i)},
\end{aligned} \tag{43}$$

in which the term $\hat{\mathbf{Q}}_{t}^{(i-1)}$ is the heat flow vector for the ROM $\hat{\Omega}_t$ in iteration $(i-1)$.

Assembling the target part interior ${}^{i}\Omega_t$ and its interface boundary ${}^{\Gamma}\Omega_t$ in Equation (43), we can obtain the non-linear thermal governing equation for the ROM $\hat{\Omega}_t$ as

$$\begin{aligned}
&\mathbf{C}_{t}^{(i)}\dot{\boldsymbol{\theta}}_{t}^{(i)} + \hat{\mathbf{k}}_{t}^{(i-1)}\Delta\boldsymbol{\theta}_{t}^{(i)} = \hat{\mathbf{Q}}_{t}^{(i-1)} \quad \text{with} \quad \hat{\mathbf{k}}_{t}^{(i-1)} = \mathbf{k}_{t}^{(i-1)} + {}^{\Gamma}\mathbf{k}_{t}^{e(i-1)},\\
&\hat{\mathbf{Q}}_{t}^{(i-1)} = {}^{i}\tilde{\mathbf{Q}}_{t}^{(\mathbf{i-1})} + {}^{\Gamma}\mathbf{Q}_{t}^{\mathbf{e}(\mathbf{i-1})},
\end{aligned} \tag{44}$$

where $\hat{\mathbf{k}}_{t}^{(i-1)}$ is the reduced conductivity matrix. Note that Equation (44) is solved using the solution scheme described after Equation (15) in Section 2.1.

3.3 ROM for the thermal elastic plastic analysis

In this section, we introduce the procedure of the thermal elastic plastic analysis using the proposed method. By the previously mentioned partitioning scheme, the welding FE model is partitioned into the target part Ω_t (with non-linear behavior) and the omitted part Ω_o (with linear behavior). In the case of the welding analysis, a small portion close to the welding heat source behaves non-linearly and the remaining portion of the FE model behaves linearly.

As described in Fig. 4, after the partitioning, we can construct the ROM $\hat{\Omega}_t$ by condensing the omitted part Ω_o (linear part) into the target part Ω_t (non-linear part) with the condensation algorithm (Guyan, 1965; Wilson, 1974). Therefore, the ROM $\hat{\Omega}_t$ will only be updated during iteration procedures of the non-linear analysis, and we can conduct the non-linear analysis more efficiently than

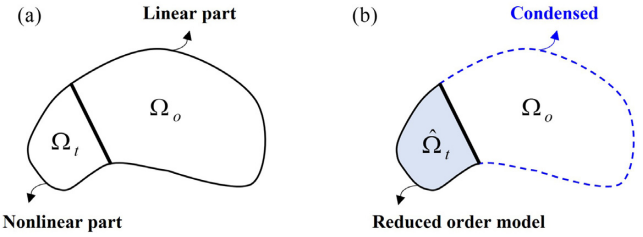

Figure 4: Construction of the mechanical ROM. (a) Partitioning of the body considering the linear and non-linearity. (b) Constructing the ROM $\hat{\Omega}_t$ by condensing the omitted part Ω_o.

using the global FE model. This is the most attractive feature of the proposed method.

Remembering the static equation described in Equation (24), and considering the partitioned equation in Equation (38), the partitioned formulation is defined as

$$\mathbf{Ku} = \mathbf{F} \text{ with } \mathbf{K} = \begin{bmatrix} \mathbf{K}_o & \mathbf{K}_{ot} \\ \mathbf{K}_{to} & \mathbf{K}_t \end{bmatrix},\ \mathbf{u} = \begin{bmatrix} \mathbf{u}_o \\ \mathbf{u}_t \end{bmatrix},\ \mathbf{F} = \begin{bmatrix} \mathbf{F}_o \\ \mathbf{F}_t \end{bmatrix}. \tag{45}$$

Compared to the number of DOFs in the target part Ω_t, there are a relatively large number of DOFs in the omitted part Ω_o. As the number of DOFs in the omitted part Ω_o becomes larger, the condensation process requires more computational time. Thus, to conduct the condensation of the omitted part Ω_o more efficiently, we use the ASC method (Boo & Lee, 2017).

As shown in Fig. 5, in the proposed method, the body is partitioned into two parts (Ω_t and Ω_o), and only Ω_o is partitioned into many substructures. After the substructuring, the coupling relationship between substructures is defined as shown in Fig. 5b. This substructural tree diagram is a computational strategy of the condensation process.

The linear static equation in Equation (45) can be expressed in the partitioned form considering n substructures for Ω_o as

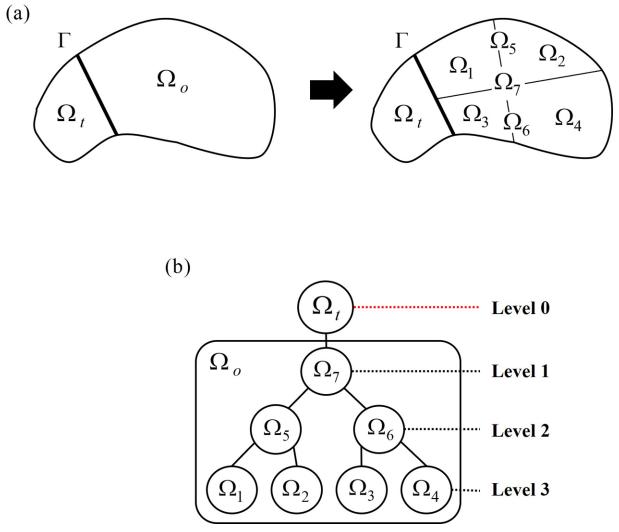

Figure 5: Substructuring and tree diagram in the proposed method. (a) Substructuring of the body. (b) Tree diagram with seven substructures in the omitted part Ω_o.

$$\mathbf{K}=\left[\begin{array}{cccc:c} \mathbf{K}_1 & \cdots & \mathbf{K}_{1,l} & \cdots & \mathbf{K}_{1,n} & \mathbf{K}_{1,t} \\ & \ddots & & & \vdots & \vdots \\ & & \mathbf{K}_k & \cdots & \mathbf{K}_{k,n} & \mathbf{K}_{k,t} \\ & sym. & & \ddots & \vdots & \vdots \\ & & & & \mathbf{K}_n & \mathbf{K}_{n,t} \\ \hdashline sym. & & & & & \mathbf{K}_t \end{array}\right], \quad \mathbf{u}=\left[\begin{array}{c} \mathbf{u}_1 \\ \vdots \\ \mathbf{u}_k \\ \vdots \\ \mathbf{u}_n \\ \mathbf{u}_t \end{array}\right], \quad \mathbf{F}=\left[\begin{array}{c} \mathbf{F}_1 \\ \vdots \\ \mathbf{F}_k \\ \vdots \\ \mathbf{F}_n \\ \hdashline \mathbf{F}_t \end{array}\right], \tag{46}$$

where $\mathbf{K}_t$, $\mathbf{u}_t$, and $\mathbf{F}_t$ are the stiffness matrix, displacement vector, and force vector, respectively, corresponding to the target part Ω_t. Here, $\mathbf{K}_{k,t}$ is the coupled stiffness matrix between the k^{th} substructure and the target part Ω_t. In the same way, we can define $\mathbf{K}_k$, $\mathbf{u}_k$, and $\mathbf{F}_k$ for the k^{th} substructure, and coupled matrix $\mathbf{K}_{k,\,l}$ between the k^{th} and l^{th} substructure.

Expanding the first row equation in Equation (46), the following equation is obtained:

$$\mathbf{K_1}\mathbf{u}_1+\sum_{l=2}^{n}\mathbf{K}_{1,l}\mathbf{u}_l+\mathbf{K}_{1,t}\mathbf{u}_t=\mathbf{F}_1, \tag{47}$$

and the displacement vector $\mathbf{u_1}$ corresponding to the first substructure is defined as

$$\mathbf{u_1}=\mathbf{K}_1^{-1}\mathbf{F_1}+\sum_{l=2}^{n}\mathbf{\Psi}_{1,l}\mathbf{u}_l+\mathbf{\Psi}_{1,t}\,\mathbf{u}_t \quad \text{with} \quad \mathbf{\Psi}_{1,l}=-\mathbf{K}_1^{-1}\mathbf{K}_{1,l},$$
$$\mathbf{\Psi}_{1,t}=-\mathbf{K}_1^{-1}\mathbf{K}_{1,t}, \tag{48}$$

where $\mathbf{\Psi}_{1,l}$ is the constraint matrix to couple the first substructure with the l^{th} substructure, and $\mathbf{\Psi}_{1,t}$ is the constraint matrix to couple the first substructure with the target part Ω_t.

Substituting $\mathbf{u}_1$ in Equation (48) into the displacement vector $\mathbf{u}$ in Equation (46), the displacement vector $\mathbf{u}$ can be rewritten as

$$\mathbf{u}=\mathbf{C}_1\mathbf{u}^{(1)}+\mathbf{F}_a^{(1)},$$

with

$$\mathbf{C}_1=\left[\begin{array}{c:ccccc} \mathbf{0} & \mathbf{\Psi}_{1,2} & \cdots & \mathbf{\Psi}_{1,l} & \cdots & \mathbf{\Psi}_{1,t} \\ \hdashline \mathbf{0} & \mathbf{I} & & & & \mathbf{0} \\ \vdots & & \ddots & & & \\ \mathbf{0} & & & \mathbf{I} & & \\ \vdots & & & & \ddots & \\ \mathbf{0} & \mathbf{0} & & & & \mathbf{I} \end{array}\right], \quad \mathbf{u}^{(1)}=\left[\begin{array}{c} \mathbf{0} \\ \hdashline \mathbf{u}_2 \\ \vdots \\ \mathbf{u}_k \\ \vdots \\ \mathbf{u}_t \end{array}\right], \quad \mathbf{F}_a^{(1)}=\left[\begin{array}{c} \mathbf{K}_1^{-1}\mathbf{F}_1 \\ \hdashline \mathbf{0} \\ \vdots \\ \mathbf{0} \\ \vdots \\ \mathbf{0} \end{array}\right], \tag{49}$$

in which $\mathbf{C}_1$ is the first condensation matrix, $\mathbf{u^{(1)}}$ is the first condensed displacement vector, and $\mathbf{F}_a^{(1)}$ is the first additional force vector.

Substituting Equations (49) into (46), we can obtain the first condensed linear static equation as follows:

$$\mathbf{K}^{(1)}\mathbf{u}^{(1)}=\mathbf{F}^{(1)} \quad \text{with} \quad \mathbf{K}^{(1)}=\mathbf{KC}_1, \quad \mathbf{F}^{(1)}=\mathbf{F}-\mathbf{KF}_a^{(1)}, \tag{50}$$

where $\mathbf{K}^{(1)}$, $\mathbf{u}^{(1)}$, and $\mathbf{F}^{(1)}$ are the first condensed stiffness matrix, displacement vector, and force vector, respectively.

From Equations (49) and (50), the partitioned formulation of Equation (50) is written as

$$\left[\begin{array}{c:ccc} \mathbf{0} & \mathbf{0} & \cdots & \mathbf{0} \\ \hdashline \mathbf{0} & \hat{\mathbf{K}}_2^{(1)} & \cdots & \hat{\mathbf{K}}_{2,t}^{(1)} \\ \vdots & & \ddots & \vdots \\ \mathbf{0} & & \hat{\mathbf{K}}_k^{(1)} & \hat{\mathbf{K}}_{k,t}^{(1)} \\ & sym. & & \hat{\mathbf{K}}_t^{(1)} \end{array}\right]\left[\begin{array}{c} \mathbf{0} \\ \hdashline \mathbf{u}_2 \\ \vdots \\ \mathbf{u}_k \\ \vdots \\ \mathbf{u}_t \end{array}\right]=\left[\begin{array}{c} \mathbf{0} \\ \hdashline \hat{\mathbf{F}}_2^{(1)} \\ \vdots \\ \hat{\mathbf{F}}_k^{(1)} \\ \vdots \\ \hat{\mathbf{F}}_t^{(1)} \end{array}\right], \tag{51}$$

in which the hat $\wedge$ denotes the updated substructural terms during the condensation procedure according to the substructural tree diagram. Note that all the submatrices of the first condensed linear static equation are updated to describe the general formulation. Here, in the case that the first substructure and the l^{th} substructure are not coupled, the constraint matrix $\mathbf{\Psi}_{1,l}$ of the first condensation matrix $\mathbf{C}_1$ becomes zero.

In the same way, after conducting the condensation procedure to the $(k-1)^{th}$ substructure, the following $(k-1)^{th}$ condensed linear static equation is obtained as

$$\left[\begin{array}{cc:cc} \mathbf{0} & \mathbf{0} & \mathbf{0} & \mathbf{0} \\ & \ddots & & \ddots \\ \mathbf{0} & \mathbf{0} & \mathbf{0} & \mathbf{0} \\ \hdashline \mathbf{0} & \mathbf{0} & \hat{\mathbf{K}}_k^{(k-1)} & \hat{\mathbf{K}}_{k,t}^{(k-1)} \\ & \ddots & & \ddots \\ \mathbf{0} & \mathbf{0} & sym. & \hat{\mathbf{K}}_t^{(k-1)} \end{array}\right]\left[\begin{array}{c} \mathbf{0} \\ \vdots \\ \mathbf{0} \\ \hdashline \mathbf{u}_k \\ \vdots \\ \mathbf{u}_t \end{array}\right]=\left[\begin{array}{c} \mathbf{0} \\ \vdots \\ \mathbf{0} \\ \hdashline \hat{\mathbf{F}}_k^{(k-1)} \\ \vdots \\ \hat{\mathbf{F}}_t^{(k-1)} \end{array}\right]. \tag{52}$$

From expanding the k^{th} row in Equation (52), the following equation is obtained:

$$\hat{\mathbf{K}}_k^{(k-1)}\mathbf{u}_k+\sum_{l=k+1}^{n}\hat{\mathbf{K}}_{k,\,l}^{(k-1)}\mathbf{u}_l+\hat{\mathbf{K}}_{k,\,t}^{(k-1)}\mathbf{u}_t=\hat{\mathbf{F}}_k^{(k-1)}, \tag{53}$$

and the displacement vector $\mathbf{u_k}$ corresponding to k^{th} substructure is defined as

$$\mathbf{u}_k=(\hat{\mathbf{K}}_k^{(k-1)})^{-1}\hat{\mathbf{F}}_k^{(k-1)}+\sum_{l=k+1}^{n}\mathbf{\Psi}_{k,\,l}\,\mathbf{u}_l+\mathbf{\Psi}_{j,\,t}\mathbf{u}_t,$$
$$\text{with} \quad \mathbf{\Psi}_{k,\,l}=-(\hat{\mathbf{K}}_k^{(k-1)})^{-1}\hat{\mathbf{K}}_{k,\,l}^{(k-1)}, \quad \mathbf{\Psi}_{k,\,t}=-(\hat{\mathbf{K}}_k^{(k-1)})^{-1}\hat{\mathbf{K}}_{k,\,t}^{(k-1)}, \tag{54}$$

where $\mathbf{\Psi}_{k,\,l}$ is the constraint matrix to couple the k^{th} substructure with the l^{th} substructure, and $\mathbf{\Psi}_{k,t}$ is the constraint matrix to couple the k^{th} substructure with the target part Ω_t.

Using Equation (54), the $(k-1)^{th}$ condensed displacement vector $\mathbf{u^{(k-1)}}$ can be rewritten as

$$\mathbf{u}^{(k-1)}=\mathbf{C}_k\mathbf{u}^{(k)}+\mathbf{F}_a^{(k)},$$

with

$$\mathbf{C}_k=\left[\begin{array}{cc:cc} \mathbf{0} & \mathbf{0} & \mathbf{0} & \mathbf{0} \\ & \ddots & & \ddots \\ \mathbf{0} & \mathbf{0} & \mathbf{\Psi}_{k,l} & \mathbf{\Psi}_{k,t} \\ \hdashline \mathbf{0} & \mathbf{0} & \mathbf{I} & \mathbf{0} \\ & \ddots & & \ddots \\ \mathbf{0} & \mathbf{0} & \mathbf{0} & \mathbf{I} \end{array}\right], \quad \mathbf{u}^{(k)}=\left[\begin{array}{c} \mathbf{0} \\ \vdots \\ \mathbf{0} \\ \hdashline \mathbf{u}_{k+1} \\ \vdots \\ \mathbf{u}_t \end{array}\right], \quad \mathbf{F}_a^{(k)}=\left[\begin{array}{c} \mathbf{0} \\ \vdots \\ (\hat{\mathbf{K}}_k^{(k-1)})^{-1}\hat{\mathbf{F}}_k^{(k-1)} \\ \hdashline \mathbf{0} \\ \vdots \\ \mathbf{0} \end{array}\right], \tag{55}$$

Table 1: Algorithm of the proposed mechanical ROM method.

Algorithm
Step 1: Load the structural system matrices ($\mathbf{K}$ and $\mathbf{F}$) in Equation (45)
Step 2: Do the algebraic multi-level substructuring by Equation (46)
Step 3: Construct the substructural tree diagram in Fig. 5b
For $k = 1, 2, \ldots n$,
Step 4: Compute condensation matrix $\mathbf{C}_k$ and additional force vector $\mathbf{F}_a^{(k)}$ in Equation (55)
Step 5: Do the k^{th} condensation procedure in Equation (56)
End for
Step 6: Compute the reduced matrices ($\tilde{\mathbf{K}}$ and $\tilde{\mathbf{F}}$) in Equation (61)

in which $\mathbf{C}_k$ is the k^{th} condensation matrix, $\mathbf{u}^{(k)}$ is the k^{th} condensed displacement vector, and $\mathbf{F}_a^{(k)}$ is the k^{th} additional force vector.

Using Equation (55) and the $(k-1)^{th}$ condensed linear static equation, we can obtain the k^{th} condensed linear static equation as follows

$$\mathbf{K}^{(k)}\mathbf{u}^{(k)} = \mathbf{F}^{(k)} \quad \text{with} \quad \mathbf{K}^{(k)} = \mathbf{K}^{(k-1)}\mathbf{C}_k, \quad \mathbf{F}^{(k)} = \mathbf{F}^{(k-1)} - \mathbf{K}^{(k-1)}\mathbf{F}_a^{(k)}, \tag{56}$$

where $\mathbf{K}^{(k)}$, $\mathbf{u}^{(k)}$ and $\mathbf{F}^{(k)}$ are the k^{th} condensed stiffness matrix, displacement vector, and force vector, respectively.

Then, the partitioned formulation of Equation (56) is written as

$$\begin{bmatrix} \mathbf{0} & & \mathbf{0} & & \mathbf{0} \\ & \ddots & & \ddots & \\ \mathbf{0} & & \mathbf{0} & & \mathbf{0} \\ \hline \mathbf{0} & & \hat{\mathbf{K}}_{k+1}^{(k)} & \cdots & \hat{\mathbf{K}}_{k+1,t}^{(k)} \\ & \ddots & & \ddots & \vdots \\ \mathbf{0} & & sym. & & \hat{\mathbf{K}}_{t}^{(k)} \end{bmatrix} \begin{bmatrix} \mathbf{0} \\ \vdots \\ \mathbf{0} \\ \hline \mathbf{u}_{k+1} \\ \vdots \\ \mathbf{u}_t \end{bmatrix} = \begin{bmatrix} \mathbf{0} \\ \vdots \\ \mathbf{0} \\ \hline \hat{\mathbf{F}}_{k+1}^{(k)} \\ \vdots \\ \hat{\mathbf{F}}_{t}^{(k)} \end{bmatrix}. \tag{57}$$

After performing all the condensation procedures, the fully (= n^{th}) condensed linear static equation is obtained as

$$\mathbf{K}^{(n)}\mathbf{u}^{(n)} = \mathbf{F}^{(n)}, \tag{58}$$

where $\mathbf{K}^{(n)}$, $\mathbf{u}^{(n)}$, and $\mathbf{F}^{(n)}$ are the n^{th} condensed stiffness matrix, displacement vector, and force vector, respectively.

The fully condensed linear static equation in Equation (58) can be expressed in the partitioned form as

$$\mathbf{K}^{(n)} = \begin{bmatrix} \mathbf{0} & & \mathbf{0} & \mathbf{0} \\ & \ddots & & \vdots \\ \mathbf{0} & & \mathbf{0} & \mathbf{0} \\ \hline \mathbf{0} & \cdots & \mathbf{0} & \hat{\mathbf{K}}_t^{(n)} \end{bmatrix}, \quad \mathbf{u}^{(n)} = \begin{bmatrix} \mathbf{0} \\ \vdots \\ \mathbf{0} \\ \hline \mathbf{u}_t \end{bmatrix}, \quad \mathbf{F}^{(n)} = \begin{bmatrix} \mathbf{0} \\ \vdots \\ \mathbf{0} \\ \hline \hat{\mathbf{F}}_t^{(n)} \end{bmatrix}, \tag{59}$$

in which $\hat{\mathbf{K}}_t^{(n)}$ and $\hat{\mathbf{F}}_t^{(n)}$ are the reduced stiffness matrix and force vector, respectively. Here, all substructural terms become zero except for the terms corresponding to the ROM of interest, $\hat{\Omega}_t$.

In Equation (59), neglecting zero substructural matrices, we can obtain the reduced linear static equation only for the ROM $\hat{\Omega}_t$ as

$$\hat{\mathbf{K}}_t^{(n)}\mathbf{u}_t = \hat{\mathbf{F}}_t^{(n)}. \tag{60}$$

Finally, we can obtain the stiffness matrix and force vector for the ROM $\hat{\Omega}_t$ as

$$\tilde{\mathbf{K}} = \hat{\mathbf{K}}_t^{(n)}, \quad \tilde{\mathbf{F}} = \hat{\mathbf{F}}_t^{(n)}, \tag{61}$$

and these can be decomposed into the original and additional parts as

$$\tilde{\mathbf{K}} = \mathbf{K}_t + \mathbf{K}_R^{(n)}, \quad \tilde{\mathbf{F}} = \mathbf{F}_t + \mathbf{F}_R^{(n)}. \tag{62}$$

in which $\mathbf{K}_t$ and $\mathbf{F}_t$ are the original stiffness matrix and force vector of the target part Ω_t before condensation, and $\mathbf{K}_R^{(n)}$ and $\mathbf{F}_R^{(n)}$ are the additional stiffness matrix and force vector resulting from the n^{th} condensation procedure for the omitted part Ω_o.

By using $\tilde{\mathbf{K}}$ and $\tilde{\mathbf{F}}$, similarly to Equation (33), the reduced governing equation of the thermal elastic plastic analysis can be defined as

$$\tilde{\mathbf{K}}\,\Delta\mathbf{u}_t = \Delta\tilde{\mathbf{F}}, \tag{63}$$

where $\Delta\mathbf{u}_t$ is the incremental nodal displacement vector for the ROM $\hat{\Omega}_t$.

Applying the Newton–Raphson iteration, we can obtain the incremental non-linear governing equation for the ROM $\hat{\Omega}_t$ as follows:

$$\tilde{\mathbf{K}}^{(j-1)}\Delta\mathbf{u}_t^{(j)} = \tilde{\mathbf{F}}^{(j)} - \tilde{\mathbf{F}}^{(j-1)}, \tag{64}$$

in which $\Delta\mathbf{u}_t^{(j)}$ is the incremental nodal displacement vector for the ROM $\hat{\Omega}_t$ in iteration j.

From Equations (35) and (37), the displacement vector $\mathbf{u}_t^{(j)}$ and the stress distributions $\boldsymbol{\sigma}_t^{(j)}$ can be calculated as

$$\mathbf{u}_t^{(j)} = \mathbf{u}_t^{(j-1)} + \Delta\mathbf{u}_t^{(j)}, \quad \boldsymbol{\sigma}_t^{(j)} = \boldsymbol{\sigma}_t^{(j-1)} + \Delta\boldsymbol{\sigma}_t^{(j)}, \tag{65}$$

in which $\Delta\boldsymbol{\sigma}_t^{(j)}$ is the incremental nodal displacement vector for the ROM $\hat{\Omega}_t$ in iteration j.

The algorithm of the proposed mechanical ROM method is summarized in Table 1. In the following sections, the performance of the proposed method is evaluated using several numerical examples.

4 Application Examples

In this section, we investigate the performance of the proposed method using two FE welding simulation problems: butt welding of mild steel pipe and plate. The flow chart of the proposed welding simulation is described in Fig. 6.

The global FE model for the welding simulation is partitioned into the target and omitted parts. Then, the thermal boundary condition is developed through a user subroutine and applied to the target part interface boundary $^{\Gamma}\Omega_t$ to construct the thermal ROM. The computer code for the ASC method is implemented to calculate the mechanical ROM, and the additional terms generated in the code are applied as initial conditions for the tar-

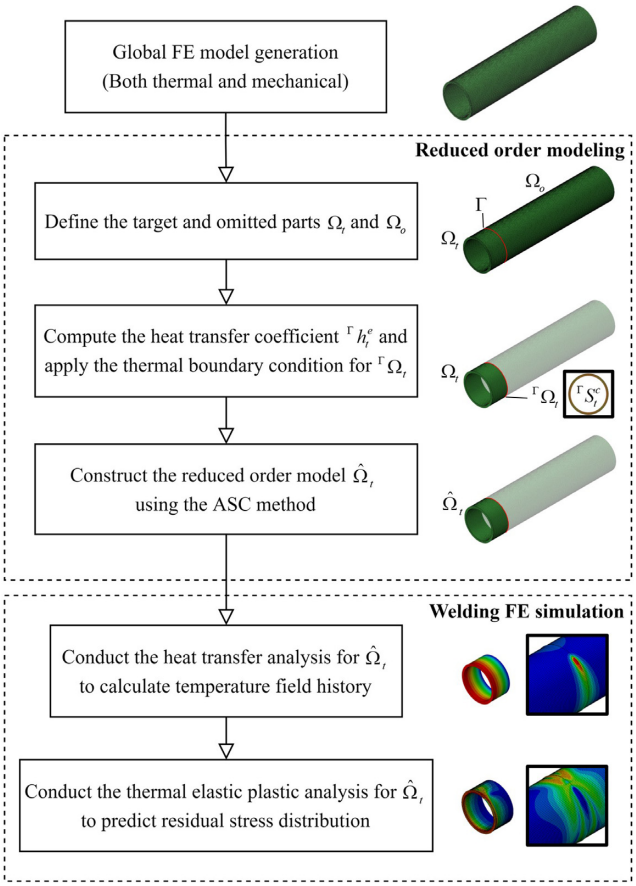

Figure 6: Flowchart of the proposed method.

get part Ω_t. Finally, the sequentially coupled heat transfer and thermal elastic plastic analyses using the ROMs are performed to obtain the temperature field history and then the displacement and stress field history.

In general, the degree of the FE shape functions in thermo-mechanical problems should be one order higher than that of the thermal analysis. This is because the temperature field calculated from the thermal analysis becomes the thermal strain field in the mechanical analysis and the strains and stresses are determined as derivatives of displacement. Nevertheless, low-order elements are preferred for the welding FE analysis since they are more effective in solving non-linear welded joint problems than higher order elements. Also, fine meshes with linear elements are recommended for brick or hexahedral elements in 3D models for plasticity (Lostado *et al.*, 2017, 2018). Therefore, in this paper, thermo-mechanical FE models are constructed using the 3D eight-node hexahedral elements with the linear shape functions to perform the welding FE simulation.

To ensure the results of the welding FE simulation, it is important to appropriately characterize the thermo-mechanical behavior of the FE model (Lostado *et al.*, 2015, 2017; Fernandez *et al.*, 2017). Any small differences between the real welding and the FE simulation can be amplified enormously due to the non-linearity. Therefore, the sensitivity analysis should be conducted with the experimental data to determine the most appropriate parameters of the welding FE model. In this study, instead of conducting the welding experiment, the practical examples were implemented by referring to the literature in which the results of the FE simulation and experiment had been correlated, and we used welding parameters identical to those in the literature (Abid *et al.*, 2005, 2009; Anca *et al.*, 2011).

The mesh quality of the FE model also significantly affects the accuracy of the results. Especially, for the welding FE simulations, the mesh quality is more important due to the high non-linearity of the welding. In addition, the complex shape of the weld beads and groove can easily degrade the mesh quality of the FE model. Therefore, the mesh quality analysis is essential for the welding FE model (Zhang *et al.*, 2004; Lostado *et al.*, 2017). In this study, the mesh quality of the FE models for the pipe and plate welding problems is evaluated using the aspect ratio. The element type of the FE models is a 3D hexahedral element and in general, the aspect ratio of the hexahedral element should be less than 10. The average aspect ratios of the FE models for the pipe and plate welding problems are 1.7 and 4.5, with the highest values of 6.7 and 5, respectively. Therefore, the FE models used in this study are appropriate for the welding FE simulations.

Since there was no thermo-mechanical contact in the pipe and plate welding problems, the contact and gravity conditions are not considered in this study. Instead, the displacement boundary conditions were employed at the edges of the FE models to restrict the rigid body motion of the FE simulations. In addition, because symmetrical models were adopted, the planes of symmetry were constrained in the normal direction of the plane.

The welding FE simulation procedures including FE modeling, sequentially coupled heat transfer and thermal elastic plastic analyses, and a user subroutine were implemented in ABAQUS code. As mentioned earlier, the 3D eight-node

Table 2: Temperature-dependent thermal properties of the mild steel used in the FE simulation.

Temperature (°C)	Thermal conductivity (W/mm/°C)	Specific heat (kJ/kg/°C)
0	51.9 E−03	486
100	51.1 E−03	486
200	48.6 E−03	498
300	44.4 E−03	515
400	42.7 E−03	536
500	39.4 E−03	557
600	35.6 E−03	586
700	31.8 E−03	619
800	26.0 E−03	691
900	26.4 E−03	695
1000	27.2 E−03	691
3000	120.0 E−03	700

hexahedral elements with a linear shape function, DC3D8R and C3D8R, were used to construct FE models for heat transfer and thermal elastic plastic analyses, respectively. The computer code for the ASC method is externally implemented by FORTRAN 90. A personal computer with the Intel i7-8700 CPU and 16GB RAM was used for computation.

To verify the solution accuracy of the proposed method, we compare the mean absolute error (MAE) of the residual stresses obtained from the global and reduced models. The value of the MAE can be calculated as follows (Lostado *et al.*, 2017):

$$\mathbf{MAE} = \frac{1}{N} \cdot \sum_{i=1}^{N} \left| (\boldsymbol{\sigma}_{global})_i - (\boldsymbol{\sigma}_{reduced})_i \right|, \tag{66}$$

where σ_{global} and $\sigma_{reduced}$ are the residual stresses obtained from the global and reduced models, respectively, and N is the number of nodes selected to represent the predicted residual stress.

4.1 Material model

The thermal and mechanical temperature-dependent material properties of mild steel (Zhang *et al.*, 2004) are listed in Tables 2 and 3, respectively. These material properties were used for both pipe and plate welding problems. In this paper, the heat effects relevant to the molten metal of the weld pool were considered as below (Abid & Qarni, 2009).

During the welding, the melting behavior of the material due to fluid flow in the weld pool has the effects of both thermal conduction and convection. It can be considered by the artificially higher value of thermal conductivity 230 $W/m\,K$ for the melting point (Andersson, 1987). This results in a relatively larger weld pool with a uniform temperature. The phase change effects of the material are modeled by the latent heat of 272 kJ/kg over the temperature range of 1480–1530°C in which the solidus and liquidus temperature of the mild steel (Lindgren, 2001), respectively.

4.2 Welding heat source model

The heat from the moving welding arc is applied as a volumetric heat source by the distributed heat flux acting on the individual elements with Goldak's double-ellipsoid model (Goldak *et al.*, 1984).

A moving welding arc heat input using the Goldak's double ellipsoid model can be expressed as

$$q_f^B(x', y', z') = \frac{6\sqrt{3} f_f Q_w}{abc_f \pi \sqrt{\pi}} \cdot e^{-3\frac{x'^2}{a^2}} \cdot e^{-3\frac{y'^2}{b^2}} \cdot e^{-3\frac{z'^2}{c_f^2}}, \tag{67}$$

$$q_r^B(x', y', z') = \frac{6\sqrt{3} f_r Q_w}{abc_r \pi \sqrt{\pi}} \cdot e^{-3\frac{x'^2}{a^2}} \cdot e^{-3\frac{y'^2}{b^2}} \cdot e^{-3\frac{z'^2}{c_r^2}}, \tag{68}$$

$$f_f + f_r = 2, \quad Q_w = UI\eta, \tag{69}$$

where q_f^B and q_r^B are the front heat source and rear heat source model, respectively, and x', y', and z' are the local coordinates of the ellipsoid model. The terms a, b, and c indicate different values related to the characteristics of the welding heat source. While f_f and f_r are the heat fraction parameters in the front and rear quadrants, respectively. Here, Q_w is the input power of the welding heat source with the specific weld parameters voltage U, current I, and arc efficiency η.

4.3 Calculation of thermal boundary conditions

The calculation of the heat transfer coefficients for a combined thermal boundary condition and the proposed thermal boundary condition is described below. A combined thermal boundary condition (Brickstad & Josefson, 1998; Deng & Murakawa, 2006) is implemented to consider the heat losses in cooling material by assuming both thermal radiation and convection from the convection surface S^c. The radiation losses and convection losses are predominant at higher temperatures near and in the weld zone, and at lower temperatures away from the weld zone, respectively.

The temperature-dependent heat transfer coefficient h^e in Equation (3) for a combined thermal boundary condition that considers both the effects of thermal radiation and convection is

Table 3: Temperature-dependent thermo-mechanical properties of the mild steel used in the FE simulation.

Temperature (°C)	Elasticity modulus (N/mm²)	Poisson's ratio	Expansion	Yield stress for $\varepsilon^p = 0$ (N/mm²)	Yield stress for $\varepsilon^p = 0.1$ (N/mm²)
0	0.206 E+06	0.296	0.117 E−04	344.64	422.64
100	0.203 E+06	0.311	0.117 E−04	331.93	409.93
200	0.201 E+06	0.330	0.122 E−04	308.30	386.30
300	0.200 E+06	0.349	0.128 E−04	276.07	342.57
400	0.165 E+06	0.367	0.133 E−04	235.22	290.22
500	0.120 E+06	0.386	0.138 E−04	185.77	230.77
600	0.600 E+05	0.405	0.144 E−04	127.71	162.71
700	0.400 E+05	0.423	0.148 E−04	68.55	96.05
800	0.300 E+05	0.442	0.148 E−04	64.35	84.35
900	0.200 E+05	0.461	0.148 E−04	45.65	60.65
1000	0.100 E+05	0.480	0.148 E−04	11.32	21.32
3000	0.100 E+05	0.480	0.148 E−04	-	-

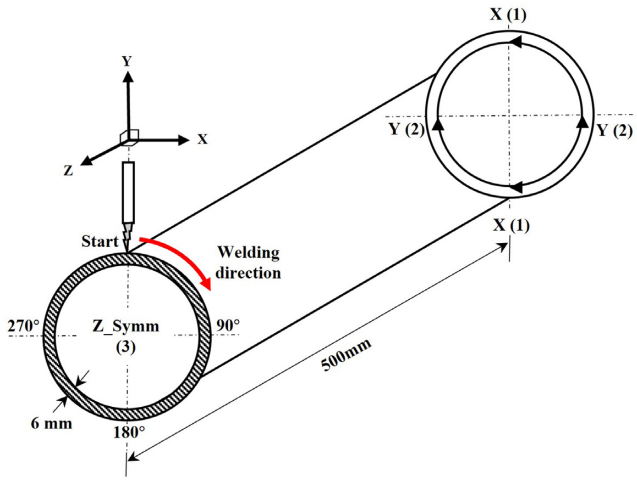

Figure 7: Definition of the pipe welding problem.

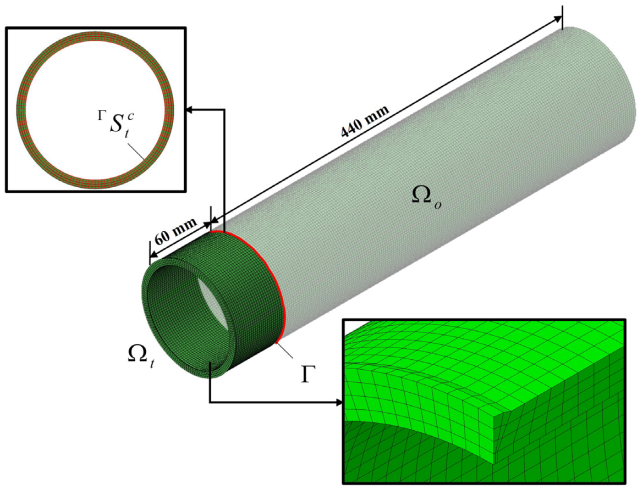

Figure 8: Meshing and partitioning of the pipe FE model.

given as

$$h^e = \begin{cases} = 0.0668\theta \times 10^{-6}\,(\mathrm{W/mm^2}) & 0 < \theta < 500^{\circ}\mathrm{C} \\ = (0.231\theta - 82.1) \times 10^{-6}\,(\mathrm{W/mm^2}) & \theta > 500^{\circ}\mathrm{C} \end{cases}, \quad (70)$$

where θ is the temperature on the convection surface S^c.

During the welding analysis, there is a temperature difference between the target and omitted parts. Note that, the welding is applied to the target part only, and the omitted part is a cooling material region. Due to this temperature difference, the continuity of temperature at the interface boundary causes heat conduction between the target and omitted parts. Here, the heat conduction can be understood as the heat loss from the target part.

On the other hand, the omitted part considers this heat conduction at the interface boundary as the heat flow input. In this study, it is assumed that the heat flow input depends on the heat convection of the omitted part. This means that the heat flow process of the omitted part is abbreviated so that the heat flow input from the target part is coupled with the heat loss due to the convection of the omitted part. Therefore, the heat transfer coefficient of the proposed thermal boundary condition is calculated using the coefficient of the combined thermal boundary condition with the areas of the interface boundary surface and the convection surface of the omitted part. Note that, the formulation of the proposed thermal boundary condition is already described in Section 3.2, and only the calculation of the heat transfer coefficient is described as follows.

Using Equation (70), the heat transfer coefficient ${}^{\Gamma}h_t^e$ in Equation (42) of the proposed thermal boundary condition is defined as

$${}^{\Gamma}h_t^e = (A_o/{}^{\Gamma}A_t) \times 0.0668\,(\theta - \theta^e) \times 10^{-6}\,(\mathrm{W/mm^2}), \quad (71)$$

in which A_o is the area of the convection surface S_o^c for the omitted part Ω_o, and ${}^{\Gamma}A_t$ is the area of the convection surface ${}^{\Gamma}S_t^c$. Here, the heat transfer coefficient ${}^{\Gamma}h_t^e$ should be less than the thermal conductivity coefficient k at the environmental temperature θ^e.

4.4 Pipe welding problem

The problem of gas metal arc welding of mild steel pipe is considered to verify the performance of the proposed method (Abid & Qarni, 2009). The model geometry, mechanical boundary conditions, and welding direction of the pipe welding problem (considered symmetrically) are detailed in Fig. 7. It has an outer diameter of 114.3 mm, a thickness of 6 mm, and a length of 500 mm. The joint type of the problem is a single "V-groove" butt joint with a 1.2 mm root gap, 60° groove angle, and 1.55 mm root face.

Table 4: Different values of the heat source parameters for the pipe welding problem.

Parameter	Value
Voltage (U)	22 V
Welding current (I)	225 A
Arc efficiency (η)	0.85
Welding speed (v)	6.25 mm/s
Width of heat source (a)	5 mm
Depth of heat source (b)	6 mm
Length of front ellipsoidal (C_f)	12.9 mm
Length of rear ellipsoidal (C_r)	10.3 mm
Front heat fraction (f_f)	1.4
Rear heat fraction (f_r)	0.6

Figure 8 shows the meshing and partitioning of the pipe FE model in detail. Because the higher temperature and flux gradients are expected around the fusion zone (FZ) and heat affected zone (HAZ), a relatively fine mesh is used, while the remaining cooling material regions have progressively coarser meshes. The smallest element is a groove element 0.3 × 1.5 × 2.5 mm, and the FE model contains 148920 nodes with 118552 connected elements. In the proposed method, the FE model is partitioned into the target part Ω_t and the omitted part Ω_o to construct the ROM $\hat{\Omega}_t$ of 19710 nodes with 15184 elements.

Table 4 presents the different values of Goldak's double ellipsoidal heat source for the pipe welding problem (Abid & Qarni, 2009). The heat source moves at constant velocity along the hoop line of the pipe at environmental temperature (25°C). As mentioned above, the moving heat source model and the thermal boundary conditions are implemented using the user subroutines DFLUX and FILM, respectively, in the ABAQUS code.

The arc shape and temperature distribution at time 52.84 s are shown in Fig. 9a, and the thermal cycles at the different points by angle on the outer surface during the welding process are shown in Fig. 9b. The results agree very well with the reference, and the temperature history at the position of 90° is almost identical to the temperature histories at 180 or 270°. Therefore, it can be concluded that the heat input gen-

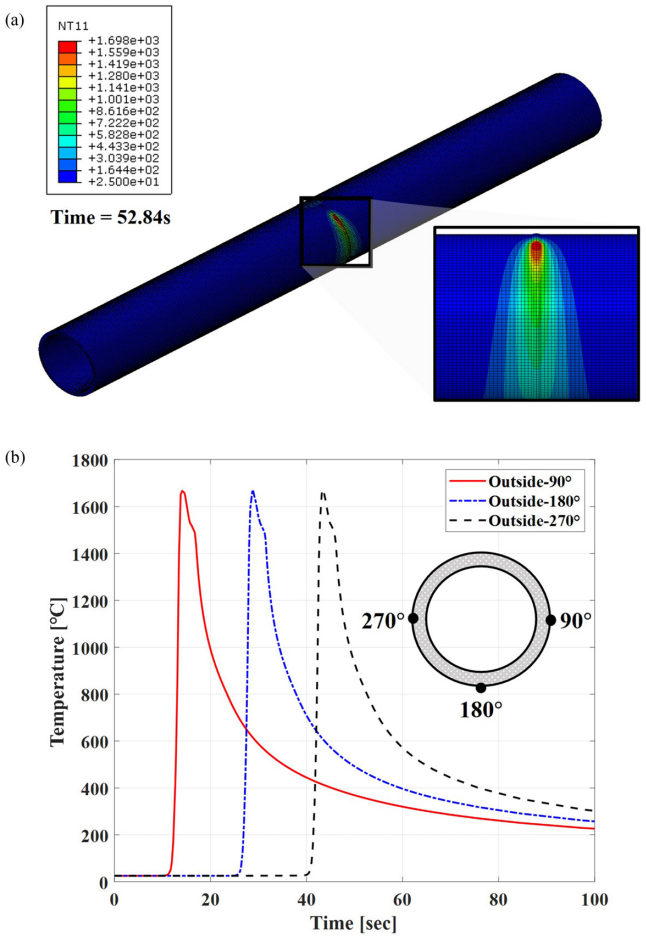

Figure 9: Temperature distribution and history of the pipe welding problem. (a) Temperature distribution at time 52.84 s. (b) Temperature history at the three locations on the outside surface.

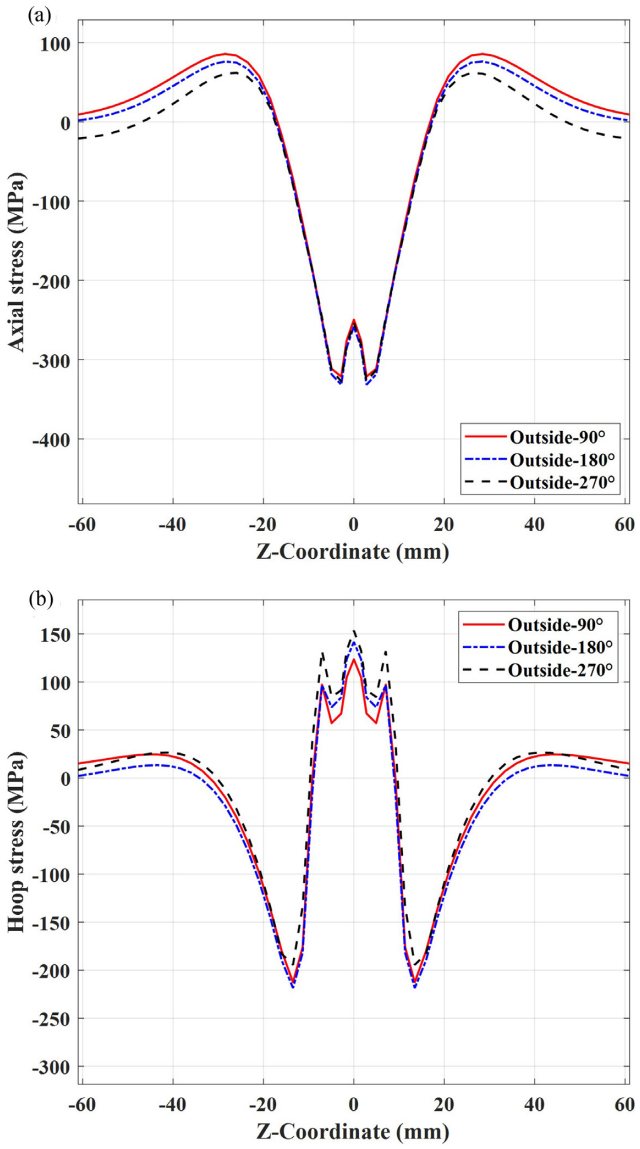

Figure 10: Residual stress distributions on the outer surface by angle. (a) Axial stress distribution. (b) Hoop stress distribution.

erated by the welding torch moving around the pipe is very constant.

Figure 10 presents the axial and hoop residual stress distributions on the outer surface with different angles, respectively. Although it can be found that the residual stresses are slightly different by angle on the outer surface, in general, both the axial stress and the hoop stress are not significantly sensitive to the angle. Thus, we compare the global and the reduced models by selecting only the results of temperature and residual stress at positions with an angle of 180°.

The contours captured along the planes of the weld cross-section at 180° of the global and reduced models are shown in Fig. 11. The temperature contours in Fig. 11a were acquired when the corresponding nodes of those planes were enduring the highest temperature. The comparison of residual stresses predicted by the global and reduced models is also shown in Fig. 11 employing stress contours of the planes. In a comparison of temperature and residual stress distributions of the global and reduced models, a good agreement was observed between them.

For a better understanding of the residual stress distributions predicted by the global and reduced models, the axial and hoop stresses of the inside and outside surfaces have been plotted along the axial direction, as shown in Fig. 12. Table 5 presents the MAEs of the residual stresses on the inside and outside surfaces at 180°. The maximum MAE for the pipe welding problem was calculated as 2.64 MPa at the hoop stress on the inside surface. Table 6 lists comparisons of the analysis times for the global and reduced models in detail, and it shows that the proposed method only requires 13.67% of the computation time compared to the global models. From the results, we can conclude that the proposed method can perform welding analysis computationally efficiently with little loss of accuracy.

4.5 Bead on the plate welding problem

In this section, a constant speed straight weld of bead on the plate problem is considered without fillers. The material proper-

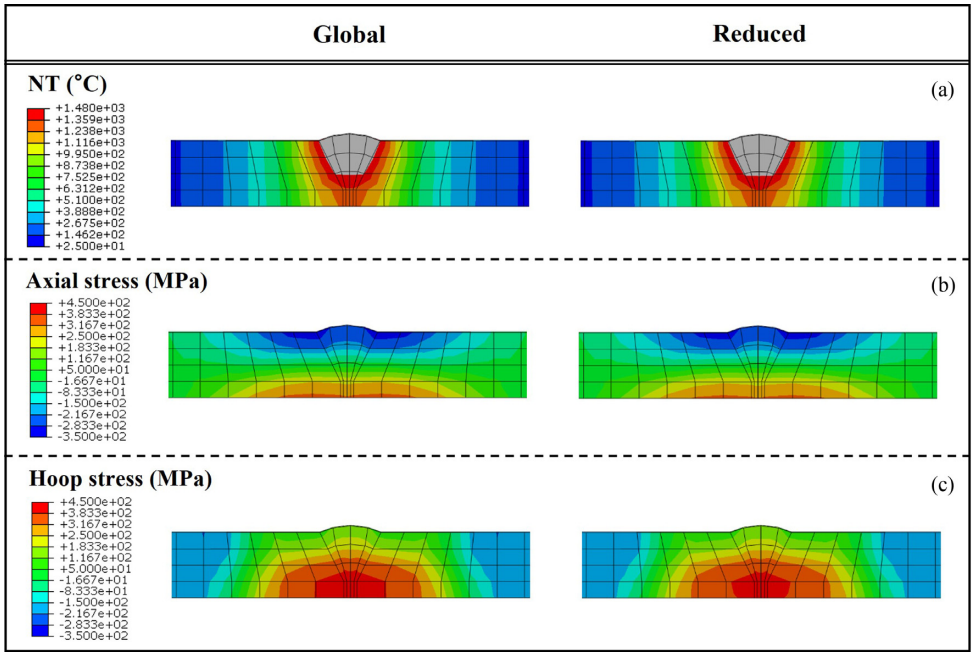

Figure 11: The temperature and residual stress contours for the pipe welding problem. (a) Temperature. (b) Axial stress. (c) Hoop stress.

Table 5: The MAEs of the axial and hoop residual stresses for the pipe welding problem.

Residual stresses	MAE (MPa)	
	Inside surface	Outside surface
Axial	1.83	1.09
Hoop	2.64	1.71

ties used in the model correspond to mild steel. The mechanical boundary conditions and the longitudinal and transverse sampling lines are shown in Fig. 13 along with the coordinate system.

Figure 14 presents the meshing and partitioning of the structural FE model. The plate FE model contains 198542 nodes with 168000 elements. A relatively fine mesh size of 1 × 1 × 2 mm for each coordinate is used around the FZ and HAZ, and the rest of the area consists of progressively coarser meshes. The proposed method was used to construct the ROM $\hat{\Omega}_t$ of 43925 nodes with 36000 elements. Table 7 presents the different values of Goldak's double ellipsoidal heat source for the plate welding problem (Anca *et al.*, 2011). The heat source moves at constant velocity along a straight line on the plate at environmental temperature (20°C). The user subroutines, DFLUX and FILM in the ABAQUS code, are used.

The temperature and residual stress contours of the global and reduced models are considered in Fig. 15. The temperature contours shown in Fig. 15a were obtained along the planes in the middle of the weld axis when the corresponding nodes in that planes withstand the highest temperature. The longitudinal and transverse residual stress contours shown in Fig. 15b and c were captured at the planes in the end and middle of the weld axis where the largest magnitude of each residual stress was found. From the contours, the longitudinal stress predicted by the reduced model was slightly different on the upper layer of the weld zone compared with the global model. However, overall, it can be observed that the results of the reduced model were closely matched with the global model.

Figure 16 presents the distribution of the longitudinal residual stress $\boldsymbol{\sigma}_z$ and transverse residual stress $\boldsymbol{\sigma}_x$ along the longitudinal and transverse sampling lines, respectively. The MAEs of the residual stresses along the sampling lines are also listed in Table 8. The maximum MAE for the plate welding problem was measured as 6.57 MPa at the transverse stress on the transverse

Table 6: Specific computational cost for the pipe welding problem.

Methods	Items	Computation times	
		(Seconds)	Ratio (%)
Global	Heat transfer analysis	47032	40.20
	Thermal elastic plastic analysis	69970	59.80
	Total	117002	100.00
Reduced	Applying the thermal boundary condition		
	Algebraic multi-level substructuring	15	0.01
	Sequential condensation procedure	475	0.41
	Heat transfer analysis for $\hat{\Omega}_t$	6431	5.50
	Thermal elastic plastic analysis for $\hat{\Omega}_t$	9072	7.75
	Total	15993	13.67

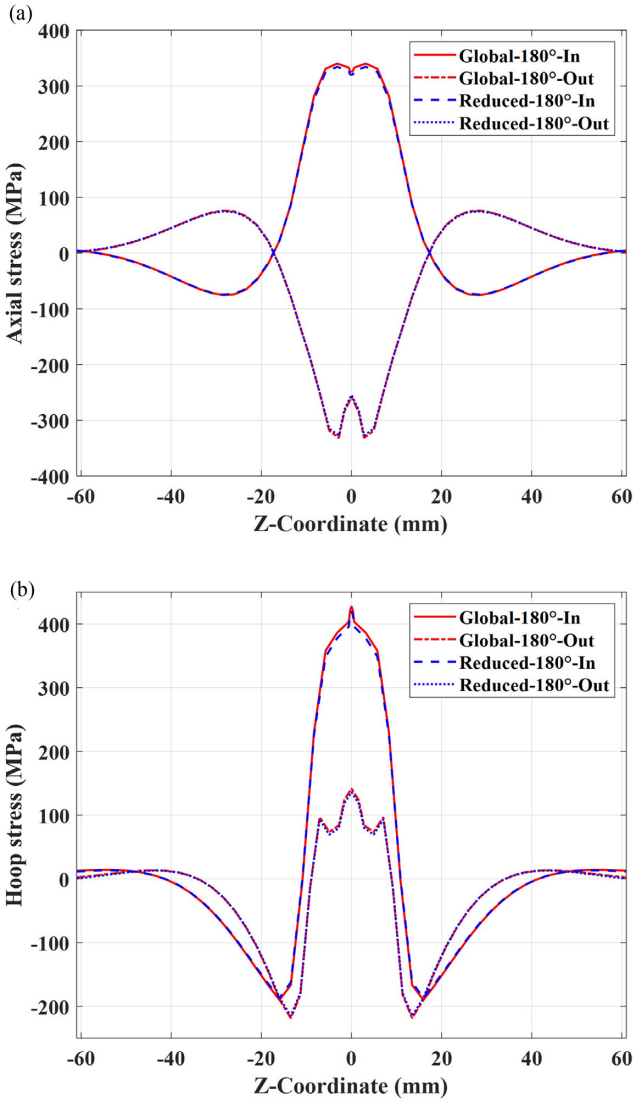

Figure 12: Residual stress distributions on inside and outside surfaces at 180° of global and reduced models. (a) Axial stress distribution. (b) Hoop stress distribution.

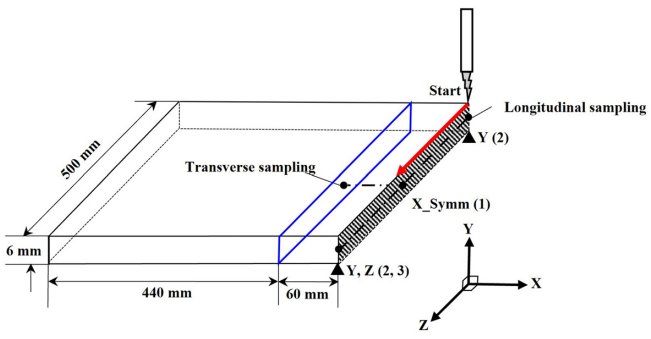

Figure 13: Bead-on-plate welding problem definition.

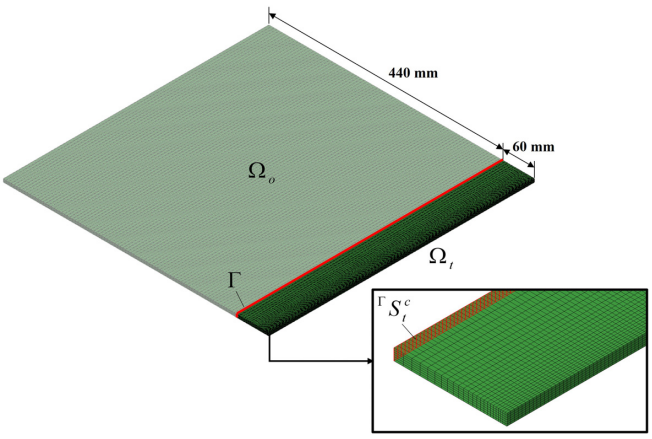

Figure 14: Meshing and partitioning of the plate FE model.

sampling line.Table 9 lists in detail the calculation time of the ROM and the sequentially coupled welding analysis. It is determined that the proposed method only needs 26.11% of the computation time required for the welding analysis using the global model. The comparison results of the global and reduced models are almost identical along the longitudinal sampling line, but the residual stresses are slightly different near the interface boundary Γ along the transverse sampling line.

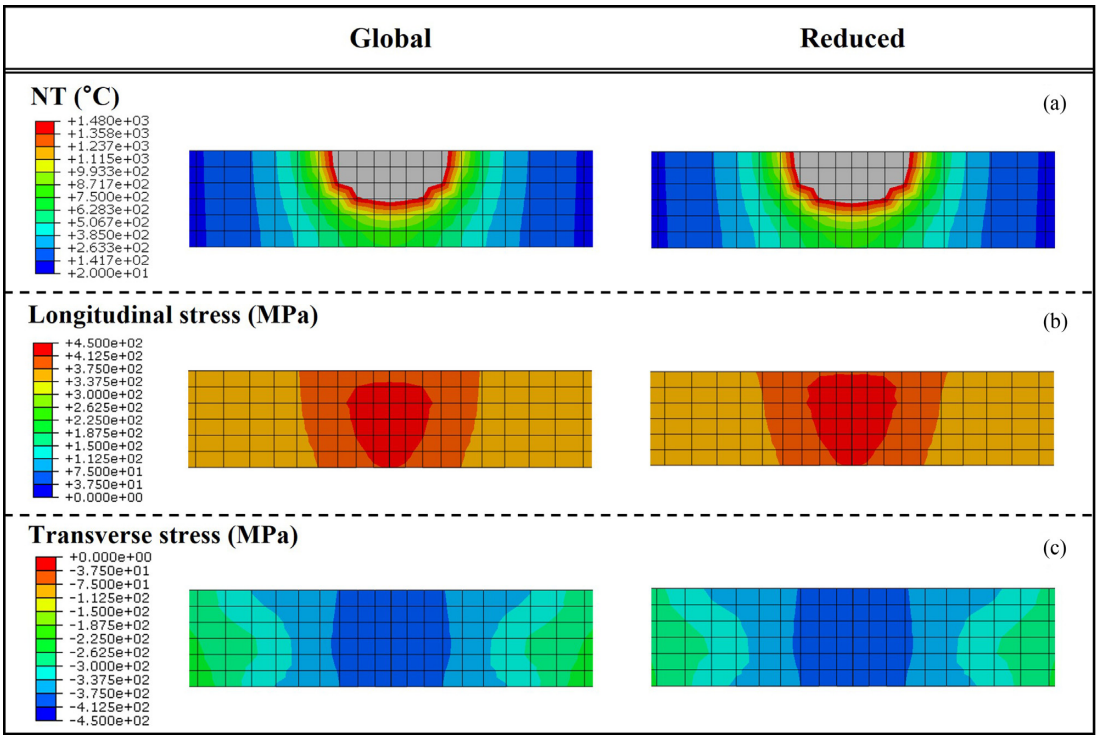

Figure 15: The temperature and residual stress contours for the plate welding problem. (a) Temperature. (b) Longitudinal stress. (c) Transverse stress.

Table 7: Different values of heat source parameters for the plate welding problem.

Parameter	Value
Voltage (U)	23 V
Welding current (I)	250 A
Arc efficiency (η)	0.825
Welding speed (v)	4.8 mm/s
Width of heat source (a)	5 mm
Depth of heat source (b)	3 mm
Length of front ellipsoidal (C_f)	5 mm
Length of rear ellipsoidal (C_r)	10 mm
Front heat fraction (f_f)	0.6
Rear heat fraction (f_r)	1.4

Table 8: The MAEs of the longitudinal and transverse residual stresses for the plate welding problem.

Residual stresses	MAE (MPa)	
	Longitudinal sampling	Transverse sampling
Longitudinal	1.54	4.64
Transverse	1.15	6.57

5 Conclusions

In this study, we proposed an efficient welding FE analysis method by adopting a ROM. The newly defined thermal boundary condition and the high-performance ROM method (i.e. the ASC method) were used to construct the thermal and mechanical ROMs, respectively. The detailed formulations were presented, and the performance of the proposed method was demonstrated in terms of accuracy and computational efficiency through butt-welding simulations for steel pipe and plate. The following conclusions can be drawn from the results.

(i) A good agreement of the transient temperature distributions between the global and reduced models was observed through the comparison of the temperature contours for the pipe and plate problems.
(ii) The residual stresses predicted by the global and reduced models showed a close match in various comparison methods. The peak error of the residual stress was observed in the hoop and transverse stresses, and it was measured by 2.6 and 6.6 MPa calculated by MAE for the pipe and plate problems, respectively. These amounts of error are 0.8 and 1.5% of the maximum residual stresses, which seem to be an acceptable level from an engineering point of view.
(iii) The computation time was about 7-times faster for the pipe welding problems and 4-times faster for the plate welding problem compared to the global models.
(iv) It would be valuable to apply the proposed method to the simulation of welded FE models with multiple-pass welds, and it is also important to develop an optimized parallel computation algorithm to solve these multiple-pass problems.

Acknowledgments

This work was supported by the National Research Foundation of Korea (NRF) grant funded by the Korea government (MSIT) (No. 2019R1C1C1004159).

Conflict of interest statement

None declared.

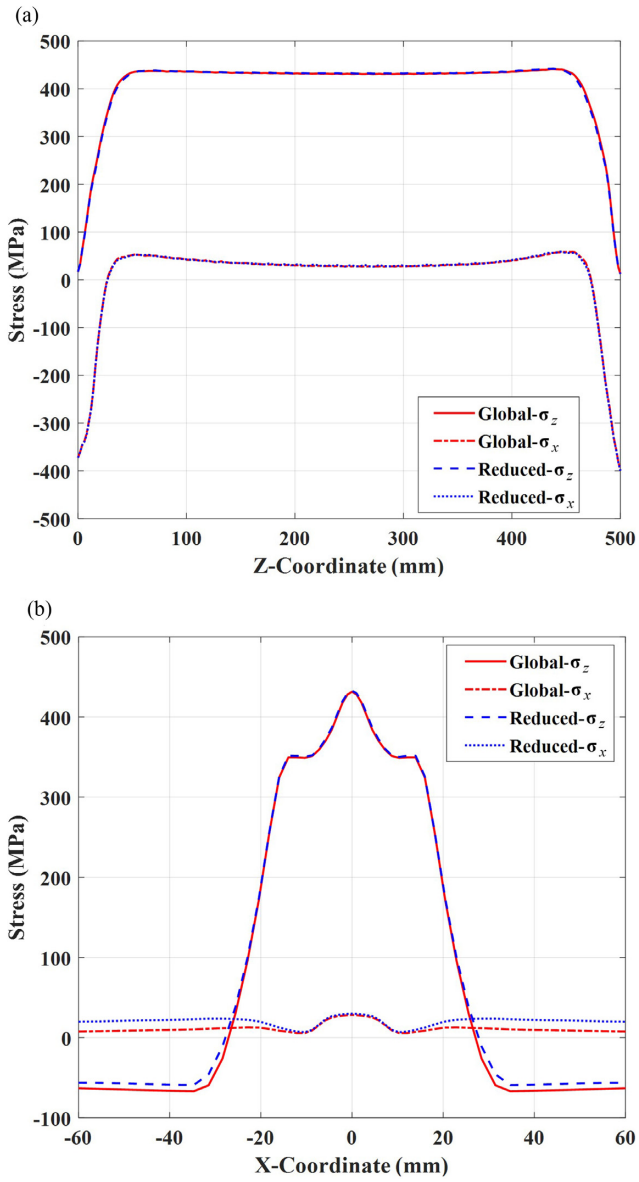

Figure 16: Longitudinal and transverse residual stresses σ_z and σ_x distributions along the sampling lines of global and reduced models. (a) Along the longitudinal sampling line. (b) Along the transverse sampling line.

References

Abid, M., & Qarni, M. J. (2009). 3D Thermal finite element analysis of single pass girth welded low carbon steel pipe–flange joints. *Turkish Journal of Engineering and Environmental Sciences*, **33**, 281–293. https://doi.org/10.3906/muh-0912-6.

Table 9: Specific computational cost for the plate welding problem.

Methods	Items	Computation times	
		(Seconds)	Ratio (%)
Global	Heat transfer analysis	189529	69.81
	Thermal elastic plastic analysis	81979	30.19
	Total	271508	100.00
Reduced	Applying the thermal boundary condition		
	Algebraic multi-level substructuring	19	0.01
	Sequential condensation procedure	1200	0.44
	Heat transfer analysis for $\hat{\Omega}_t$	40094	14.77
	Thermal elastic plastic analysis for $\hat{\Omega}_t$	29594	10.90
	Total	70907	26.11

Abid, M., Siddique, M., & Mufti, R. (2005). Prediction of welding distortions and residual stresses in a pipe–flange joint using the finite element technique. *Modelling and Simulation in Materials Science and Engineering*, **13**, 455. https://doi.org/10.1088/0965-0393/13/3/013.

Anca, A., Cardona, A., Risso, J., & Fachinotti, V. (2011). Finite element modeling of welding processes. *Applied Mathematical Modelling*, **35**, 688–707. https://doi.org/10.1016/j.apm.2010.07.026.

Andersson, B. (1987). Thermal stresses in a submerged–arc welded joint considering phase transformation. *Journal of Engineering Materials and Technology*, **100**, 356–362. https://doi.org/10.1115/1.3443504.

Bathe, K. J. (2006). *Finite element procedure*. Prentice Hall.

Bennighof, J. K., & Lehoucq, R. B. (2004). An automated multilevel substructuring method for eigenspace computation in linear elastodynamics. *SIAM Journal on Scientific Computing*, **25**, 2084–2106. https://doi.org/10.1137/S1064827502400650.

Bhatti, A. A., Barsoum, Z., & Khurshid, M. (2014). Development of a finite element simulation framework for the prediction of residual stresses in large welded structures. *Computers & Structures*, **133**, 1–11. https://doi.org/10.1016/j.compstruc.2013.11.011.

Boo, S. H., Kim, J. G., & Lee, P. S. (2015). Error estimation for the automated multi-level substructuring method. *International Journal for Numerical Methods in Engineering*, **106**, 927–950. https://doi.org/10.1002/nme.5161.

Boo, S. H., Kim, J. G., & Lee, P. S. (2016). A simplified error estimator for the CB method and its application to error control. *Computers & Structures*, **164**, 53–62. https://doi.org/10.1016/j.compstruc.2015.11.003.

Boo, S. H., & Lee, P. S. (2017). A dynamic condensation method using algebraic substructuring. *International Journal for Numerical Methods in Engineering*, **109**, 1701–1720. https://doi.org/10.1002/nme.5349.

Boo, S. H., & Oh, M. H. (2017). Automated static condensation method for local analysis of large finite element models. *Structural Engineering and Mechanics*, **61**, 807–816. https://doi.org/10.12989/sem.2017.61.6.807.

Brickstad, B., & Josefson, B. L. (1998). A parametric study of residual stresses in multi–pass butt–welded stainless steel pipes. *International Journal of Pressure Vessels and Piping*, **75**, 11–25. https://doi.org/10.1016/S0308-0161(97)00117-8.

Deng, D., & Murakawa, H. (2006). Numerical simulation of temperature field and residual stress in multi-pass welds in stainless steel pipe and comparison with experimental measurements. *Computational Materials Science*, **37**, 269–277. https://doi.org/10.1016/j.commatsci.2005.07.007.

Fernandez, R., Lostado, R., Corral Bobadilla, M., Escribano, R., Somovilla Gómez, F., & Vergara, E. (2017). Adjust the thermo-mechanical properties of finite element models welded joints based on soft computing techniques. *Lecture Notes in Computer Science*, **10334**, 699–709. https://doi.org/10.1007/978-3-319-59650-1_59.

Giri, A., Pandey, C., Mahapatra, M. M., Sharma, K., & Singh, P. K. (2015). On the estimation of error in measuring the residual stress by strain gauge rosette. *Measurement*, **65**, 41–49. https://doi.org/10.1016/j.measurement.2014.12.047.

Goldak, J., Chakravarti, A., & Bibby, M. (1984). A new finite element model for welding heat sources. *Metallurgical Transactions B*, **15**, 299–305. https://doi.org/10.1007/BF02667333.

Guirao, J., Rodríguez, E., Bayón, A., & Jones, L. (2009). Use of a new methodology for prediction of weld distortion and residual stresses using FE simulation applied to ITER vacuum vessel manufacture. *Fusion Engineering and Design*, **84**, 2187–2196. https://doi.org/10.1016/j.fusengdes.2009.04.009.

Guyan, R. J. (1965). Reduction of stiffness and mass matrices. *AIAAJ*, **3**, 380. https://doi.org/10.2514/3.2874.

Kawaguchi, A., Itoh, S., Mochizuki, M., & Kameyama, M. (2011). Large scale computation of welding residual stresses. *Progress in Nuclear Science and Technology*, **2**, 613–619.

Kumar, S., Yadav, V. K., Sharma, S. K., Pandey, C., Goyal, A., & Kumar, P. (2021). Role of dissimilar Ni-based ERNiCrMo-3 filler on the microstructure, mechanical properties and weld induced residual stresses of the ferritic/martensitic P91 steel welds joint. *International Journal of Pressure Vessels and Piping*, **193**, 104443. https://doi.org/10.1016/j.ijpvp.2021.104443.

Lindgren, L. E. (2001). Finite element modeling and simulation of welding. Part 2: Improved material modeling. *Journal of Thermal Stresses*, **24**, 195–231. https://doi.org/10.1080/01495730130000638 0.

Lostado, R., Bobadilla, M. C., Martínez Calvo, M. A., & Villanueva Roldán, P. M.. (2017). Residual stresses with time-independent cyclic plasticity in finite element analysis of welded joints. *Metals*, **7**, 136. https://doi.org/10.3390/met7040136.

Lostado, R., Escribano, R., Fernandez, R., & Martínez, M. Á. (2018). Using genetic algorithms with multi-objective optimization to adjust finite element models of welded joints. *Metals*, **8**, 230. https://doi.org/10.3390/met8040230.

Lostado, R., Fernandez, R., Mac Donald, B. J., & Villanueva, P. M. (2015). Combining soft computing techniques and the finite element method to design and optimize complex welded products. *Integrated Computer Aided Engineering*, **22**, 153–170. https://doi.org/10.3233/ICA-150484.

Mojtahedi, A., Hokmabady, H., Yaghoubzadeh, A., & Mohammadyzadeh, S. (2020). An improved model reduction-modal based method for model updating and health monitoring of an offshore jacket-type platform. *Ocean Engineering*, **209**, 107495. https://doi.org/10.1016/j.oceaneng.2020.107495.

MSC Nastran (2014). *Superelements user's guide*. MSC Software Corporation.

Murakawa, H., Ma, N., & Huang, H. (2015). Iterative substructure method employing concept of inherent strain for large-scale welding problems. *Welding in the World*, **59**, 53–63. https://doi.org/10.1007/s40194-014-0178-z.

Pandey, C., Giri, A., & Mahapatra, M. M. (2016). On the prediction of effect of direction of welding on bead geometry and residual deformation of double-sided fillet welds. *International Journal of Steel Structures*, **16**, 333–345. https://doi.org/10.1007/s13296-016-6007-z.

Pandey, C., Mahapatra, M. M., Kumar, P., & Saini, N. (2018). Effect of weld consumable conditioning on the diffusible hydrogen and subsequent residual stress and flexural strength of multipass welded P91 steels. *Metallurgical and Materials Transactions B*, **49**, 2881–2895. https://doi.org/10.1007/S11663-018-1314-8.

Roy, A., Nabi, M., & Rahman, N. (2021). Finite element compatible matrix interpolation for parametric model order reduction of electrothermal microgripper. *Journal of Computational Design and Engineering*, **8**, 1622–1635. https://doi.org/10.1093/jcde/qwab066.

Sauraw, A., Sharma, A. K., Fydrych, D., Sirohi, S., Gupta, A., Świerczyńska, A., Pandey, C., & Rogalski, G. (2021). Study on microstructural characterization, mechanical properties and residual stress of GTAW dissimilar joints of P91 and P22 steels. *Materials*, **14**, 6591. https://doi.org/10.3390/ma14216591.

Seo, H. D., & Lee, J. M. (2021). Novel welding distortion analysis method for large welded structures using orthotropic thermal expansion coefficients. *Journal of Computational Design and Engineering*, **8**, 1115–1124. https://doi.org/10.1093/jcde/qwab035.

Shanghvi, J. Y., & Michaleris, P. (2002). Thermo-elasto-plastic finite element analysis of quasi-state processes in Eulerian reference frames. *International Journal for Numerical Methods in Engineering*, **53**, 1533–1556345. https://doi.org/10.1002/nme.345.

Taraphdar, P. K., Kumar, R., Pandey, C., & Mahapatra, M. M. (2021). Significance of finite element models and solid-state phase transformation on the evaluation of weld induced residual stresses. *Metals and Materials International*, **27**, 3478–3492. https://doi.org/10.1007/s12540-020-00921-4.

Taraphdar, P. K., Thakare, J. G., Pandey, C., & Mahapatra, M. M. (2020). Novel residual stress measurement technique to evaluate through thickness residual stress fields. *Materials Letters*, **277**, 128347. https://doi.org/10.1016/j.matlet.2020.128347.

Ueda, Y., & Yamakawa, T. (1971). Analysis of thermal elastic-plastic stress and strain during welding by finite element method. *Transactions of the Japan Welding Society*, **2**, 186–196. https://doi.org/10.2207/qjjws1943.42.567.

Wang, Y. X., Zhang, P., Hou, Z. G., & Li, C. Z. (2008). Inherent strain method and thermal elastic-plastic analysis of welding deformation of a thin-wall beam. *Journal of Mechanics*, **24**, 301–309. https://doi.org/10.1017/S1727719100002434.

Wilson, E. L. (1974). The static condensation algorithm. *International Journal for Numerical Methods in Engineering*, **8**, 198–203. https://doi.org/10.1002/nme.1620080115.

Zhang, L., Reutzel, E. W., & Michaleris, P. (2004). Finite element modeling discretization requirements for the laser forming process. *International Journal of Mechanical Sciences*, **46**, 623–637. https://doi.org/10.1016/j.ijmecsci.2004.04.001.

Zheng, Z., Wang, Y., & Williams, F. (1999). Direct spectral fatigue analysis method for offshore structures. *International Journal of Offshore and Polar Engineering*, **9**, 55–61.